minerals

MDPI

Article

Genesis of Volcanic Rocks in the Zijinshan Ore District, SE China: Implications for Porphyry-Epithermal Mineralization

Zheng-Zheng Feng [1,2], Zhong-Jie Bai [1,*], Hong Zhong [1,2], Wei-Guang Zhu [1] and Shi-Ji Zheng [1]

[1] State Key Laboratory of Ore Deposit Geochemistry, Institute of Geochemistry, Chinese Academy of Sciences, Guiyang 550081, China; fengzhengzheng@mail.gyig.ac.cn (Z.-Z.F.); zhonghong@vip.gyig.ac.cn (H.Z.); zhuweiguang@vip.gyig.ac.cn (W.-G.Z.); zhengshiji@mail.gyig.ac.cn (S.-J.Z.)

[2] University of Chinese Academy of Sciences, Beijing 100049, China

* Correspondence: baizhongjie@vip.gyig.ac.cn

Received: 20 January 2020; Accepted: 20 February 2020; Published: 24 February 2020

Abstract: Volcanic rocks, as the extrusive counterparts of the mineralized intrusions, can provide important information on the magma source, petrogenesis, and metallogenic conditions of the coeval porphyry-epithermal system. Shanghang Basin volcanic rocks are spatially and temporally related to a series of adjacent porphyry-epithermal Cu–Au deposits, and they can be used as a window to study the related deposits. Two laser-ablation–inductively coupled plasma–mass spectrometry zircon U–Pb analyses of the volcanic rocks yield weighted mean ages of ~105 Ma, identical to the age of the coeval porphyry-epithermal mineralization. Rocks have SiO_2 contents of 55.4 to 74.8 wt % and belong to the high-K to shoshonitic series, characterized by strong differentiation of light rare-earth elements (REEs) relative to heavy REEs (mean La_N/Yb_N = 16.88); enrichment in light REEs, Rb, Th, and U; and depletion in Nb, Ta, Zr, Hf, and Ti. The volcanic rocks display $(^{87}Sr/^{86}Sr)_i$ values of 0.709341 to 0.711610, $\varepsilon_{Nd}(t)$ values of −6.9 to −3.3 $\varepsilon_{Hf}(t)$ values of −3.95 to −0.30, and $\delta^{18}O$ values of 6.07‰–6.79‰, suggesting that the parental magmas were derived from a mantle source enriched by subduction-related progress. SiO_2 content shows a strong negative correlation with the contents of some major and trace elements, indicating that fractional crystallization played an important role in the generation of these rocks. A binary mixing model of Hf–O isotopes gives an estimated degree of crustal contamination of 30%. In addition, magnetite crystallized early, and the samples showed high zircon Eu_N/Eu_N^* values (0.48–0.68), indicating that the parental magma had a high oxygen fugacity. The inferred suppression of plagioclase crystallization and increasing hornblende crystallization during magma evolution suggest that the magma was water rich. The high-water content and high oxygen fugacity of the magma promoted the dissolving of sulfides containing Cu and Au in the source area and contributed to the migration of ore-forming elements.

Keywords: Shimaoshan Group volcanic rocks; porphyry-epithermal Cu–Au deposit; Sr–Nd–Hf–O isotopes; Zijinshan ore district; Shanghang Basin

1. Introduction

The Zijinshan ore district is located in southwestern Fujian Province, southeastern China (Figure 1) and is one of the most important copper-, gold-, and molybdenum-producing areas in the country. Proven reserves of gold, silver, copper, and molybdenum exceed 400 tons, 6000 tons, 4.1 million tons, and 0.11 million tons, respectively [1]. It is generally considered that the copper-gold-molybdenum mineralization was associated with large-scale magmatic and hydrothermal activities during the Late Mesozoic, with most of these deposits having formed during the Cretaceous [2–5]. The Zijinshan ore district is widely regarded as a typical porphyry-epithermal metallogenic system [6–9]. The district

includes the Zijinshan high-sulfur epithermal copper-gold deposit, the Yueyang low-sulfur epithermal silver-gold-dominated polymetallic deposit, and the Luoboling porphyry copper-molybdenum deposit (Figure 2).

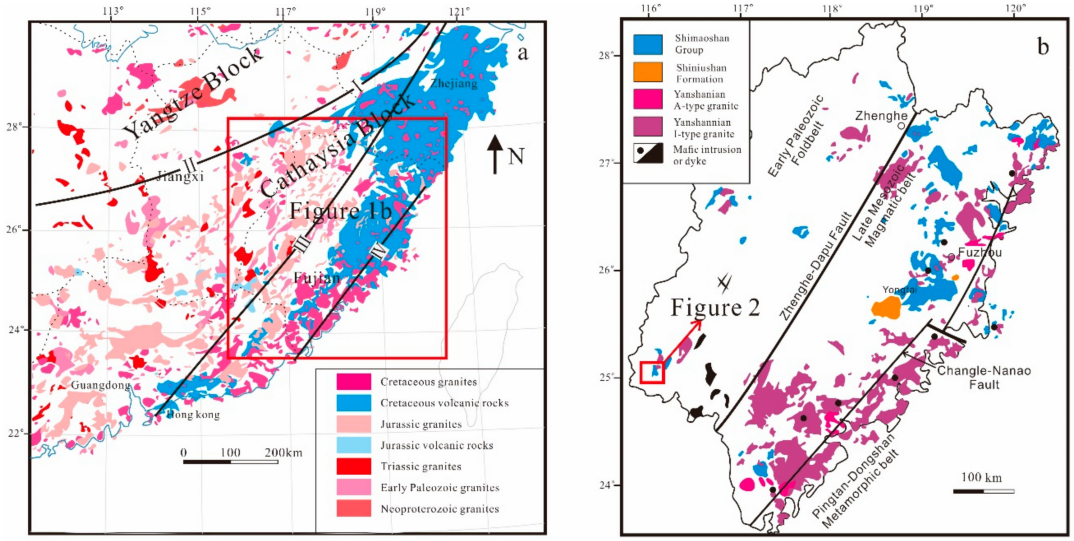

Figure 1. (**a**) Schematic geological map of South China showing the distribution of Mesozoic granitoids and volcanic rocks, modified from [10]. I—Jiangshan-Shaoxing Fault; II—Pingxiang-Yushan Fault; III—Zhenghe-Dapu Fault; IV—Changle-Nanao Fault. (**b**) Geological map depicting the distribution of Cretaceous magmatism in Fujian Province, modified from [11].

Previous studies have focused mainly on the mineralization process of the deposit and the structure of the ore field [7,12–16], whereas little attention has been paid to the source, nature, and evolution of the parental magma from which these deposits were formed. Recent studies have suggested that the Luoboling porphyry copper-molybdenum deposit and the Zijinshan copper-gold deposit were produced by discrete magmatic-hydrothermal systems [17], but the nature of the ore-forming magma associated with the Zijinshan copper-gold deposit is still unclear. However, in the Shanghang Basin, which lies adjacent to the southwest of the Zijinshan ore district (Figure 2), the porphyry-epithermal Cu–Au deposits are spatially and temporally related to the volcanic rocks of the Shimaoshan Group [18]. The volcanic rocks are considered as the extrusive magmatic counterpart of the mineralized rocks, and their study should therefore provide important new information on the magma source, petrogenesis, and metallogenic conditions of the porphyry-epithermal system at Zijinshan.

Shimaoshan Group volcanic rocks are exposed in parts of the Zijinshan ore district but are distributed mainly in the Shanghang Basin (Figure 2). Two periods of magmatic activity occurred in the vicinity of the Zijinshan ore district, at ~165–150 Ma and ~113–95 Ma [5,19–21]. The ages of formation of these deposits are well established, including the Zijinshan epithermal copper-gold deposit at 102.86 ± 0.61 Ma [17] and the Luoboling porphyry copper-molybdenum deposit at 104.9 ± 1.6 Ma [2]. Clearly, there is a close temporal and spatial relationship between the Shimaoshan Group volcanic rocks and deposits of the Zijinshan ore district. In this paper, we report new zircon U–Pb ages; trace elements, Hf–O isotopes, and whole-rock major; and trace elements and Sr–Nd isotopes of Shimaoshan Group volcanic rocks to better constrain the nature of the magma (including mantle sources) and mineralization conditions (including magma water content and oxygen fugacity) associated with the formation of the Zijinshan ore district.

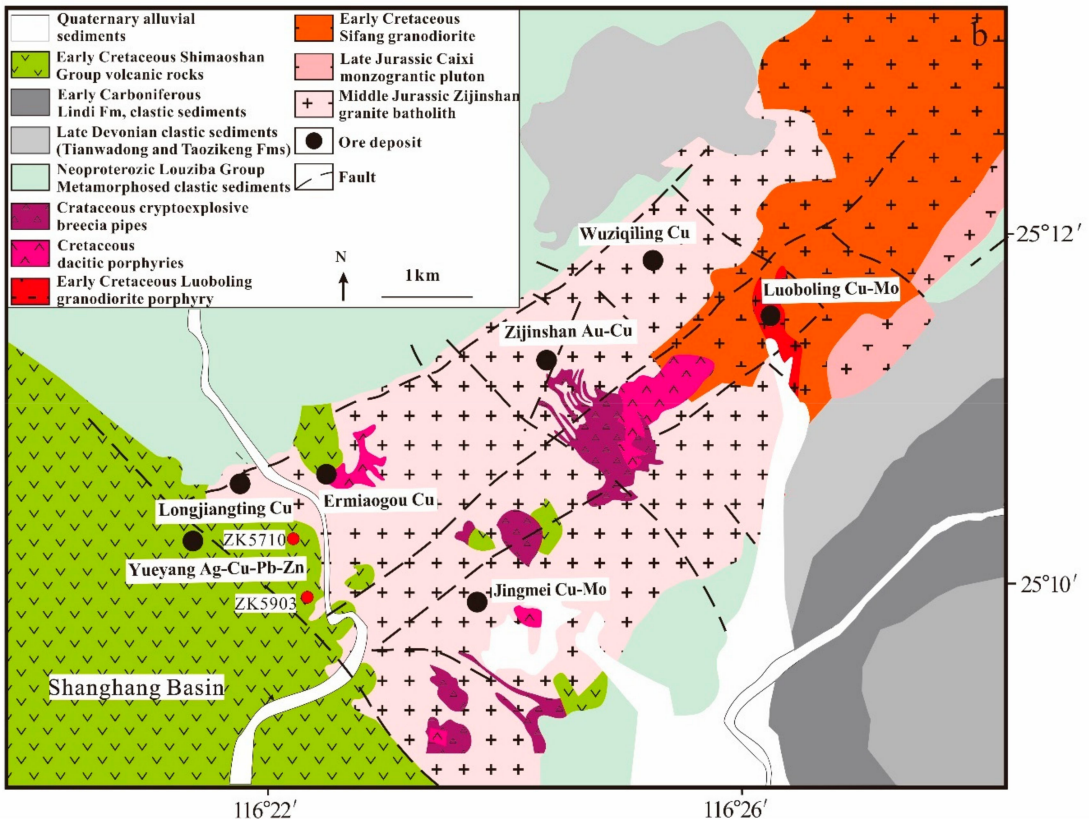

Figure 2. Geological map of the Zijinshan Cu–Au ore district showing a cluster of porphyry Cu–Mo and porphyry-epithermal Au–Cu deposits, modified from [12,19].

2. Geological Background and Sampling

Southeastern China comprises the Cathaysia Block in the southeast and the Yangtze Block in the northwest [22,23]. According to the different crustal evolutions on opposing sides of the Zhenghe-Dapu Fault, the Cathaysia Block can be further divided into the Western Cathaysia and Eastern Cathaysia regions [24,25]. Magmatic activity in southeastern China during the Late Mesozoic was concentrated mainly in the Cathaysia Block, where it migrated seaward over time and increased in intensity [10,26,27]. Volcanic–intrusive magmatism during the Yanshanian (65–220 Ma) produced mainly felsic rocks with some basalts and rare intermediate rocks [28–30]. Compared with the Jurassic, there are fewer Cretaceous granitoid rocks but more abundant volcanic rocks [10,30,31]. Jurassic volcanic rocks and granitoids are distributed mostly in Western Cathaysia, whereas Cretaceous basaltic rocks and granitoids appear mainly in Eastern Cathaysia [4,32] (Figure 1a).

Fujian Province, located in the eastern part of southeastern China, is divided into three tectonic belts by the Changle-Nanao and Zhenghe-Dapu faults. From east to west, these belts are the Pingtan-Dongshan Metamorphic Belt, the Yanshanian Magmatic Belt, and the Early Paleozoic Fold Belt [20,33,34] (Figure 1b). The Cretaceous volcanic rocks in Fujian Province can be divided into upper series named the Shimaoshan Group and lower series named the Moshishan Group, with most of the volcanic rocks in the Shanghang Basin belonging to the Shimaoshan Group. The Shimaoshan Group comprises the Huangkeng Formation and the overlying Zhaixia Formation, with each formation being further divided into upper and lower members.

The Huangkeng and Zhaixia formations of the Shimaoshan Group show substantial variation in thickness between areas of tectonic subsidence and areas of tectonic uplift [21]. The thickness of the Huangkeng Formation in areas of tectonic subsidence reaches 700 m, whereas in areas of tectonic uplift, the rocks of this formation are scattered across the Ermiaogou, and Zijinshan ore districts with a thickness of only tens to a few hundreds of meters. Rocks of the lower member of the Huangkeng

Formation comprise mostly conglomerate, glutenite, and siltstone, mixed with purple-gray dacite in the middle, and have a total thickness of about 230 m. The lower member unconformably overlies the Zijinshan Complex in the Yueyang mining area and the Louziba Group in the Ermiaogou mining area. The upper member of the Huangkeng Formation is composed of purple-gray andesite, andesitic breccia, light-gray dacitic crystal tuff, and dark-gray andesite basalt, with a total thickness of >350 m [35]. The Zhaixia Formation is distributed mainly in the southwest part of the Zijinshan ore district. Its lower member is composed of thin layers of purple-red silty mudstone intercalated with purple-red rhyolitic sedimentary tuff and rhyolitic crystal tuff, with a total thickness of up to 372 m. The upper member consists mostly of gray-white rhyolite, purple-red volcanic breccia, and rhyolitic breccia tuff, with a total thickness of up to 1037 m [35].

The ages of volcanic rocks of the Shimaoshan Group are well established [21,36,37]. By combining multiple dating methods (such as zircon LA-ICP-MS, whole-rock Rb-Sr isochron, zircon SHRIMP), estimates of the formation age of the Huangkeng Formation volcanic rocks are clustered within 93–125 Ma and those of the Zhaixia Formation within 93–121 Ma [37]. The formation age of Shimaoshan Group volcanic rocks was constrained to 104–94 Ma by using laser ablation inductively coupled plasma mass spectrometry (LA–ICP–MS) zircon U–Pb dating [36]. A whole-rock Rb–Sr isochron age of rhyolite in the Zhaixia Formation of 94 ± 7.7 Ma and an age of dacite in the Huangkeng Formation of 125 ± 9.8 Ma were reported [38]. Zircon U–Pb dating of purplish-red rhyolite and breccia from the Huangkeng Formation has yielded ages of 110.1 ± 0.7 Ma and 113.0 ± 1.9 Ma, respectively [21]. Zircon U–Pb dating of dacite and tuff in the Zijinshan ore district has given ages of 110 ± 1 Ma and 111 ± 1 Ma, respectively [19]. Zircon U–Pb ages were obtained for limestone and rhyolite in the Yueyang mining area of 105 ± 1 Ma and 102 ± 1 Ma, respectively [39]. The above data together indicate that Cretaceous magmatism in the Zijinshan ore district lasted for about 20 Myr.

Samples for this study were obtained from the Zijinshan ore district and the Shanghang Basin. The Shanghang Basin is controlled by a NW-trending fault with an area of 100 km^2. The southwestern and northeastern margins of this basin are controlled by deep NW-trending faults (Figure 2) [18]. The Shimaoshan Group, mainly the upper member of the Huangkeng Formation, is exposed in the Shanghang Basin with a thickness of >350 m. Most of the samples for this study were collected from drill cores (ZK5710 and ZK5903), with a smaller number of samples being obtained from surface exposures. A total of 62 rock samples were collected, combining the characteristics of hand specimens and the characteristics of major elements; we divided them into three categories, namely, trachyte, trachyandesite, and rhyolite-dacite, respectively. Most of the volcanic rock samples have undergone variable degrees of alteration. We have selected a more representative sample for a brief introduction from each category. Rhyolite is pink with a patchy structure (Figure 3a), in which the phenocrysts are mainly alkaline feldspar and the matrix is cryptocrystalline (Figure 3b). Trachyte is dark gray with a patchy structure and contains phenocrysts of mainly feldspar and subordinate amphibole (Figure 3c,d). Trachyandesite is dark gray, with phenocrysts of mainly plagioclase and subordinate magnetite in a matrix of grains with a preferred orientation (Figure 3e,f).

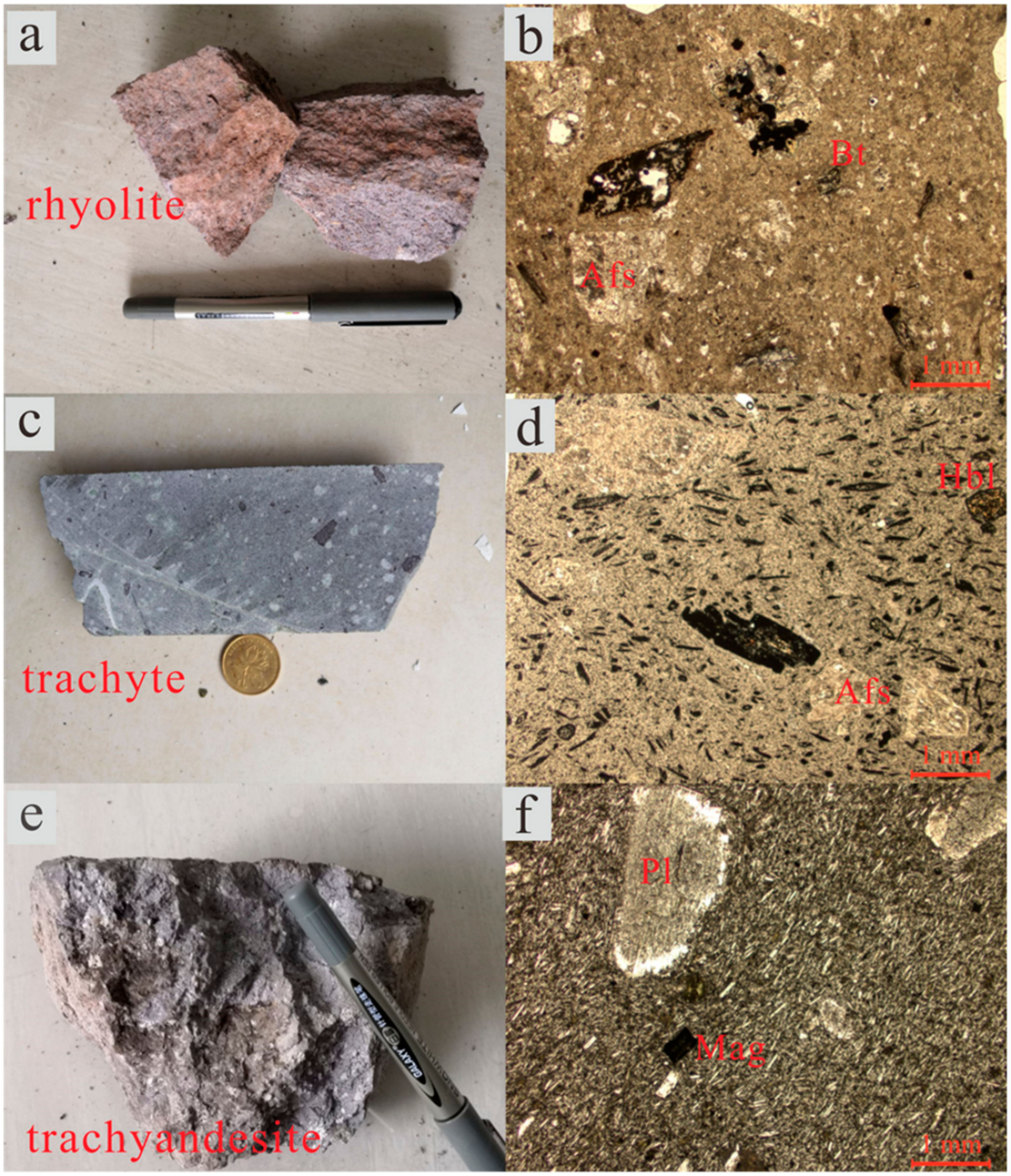

Figure 3. Photographs of rock hand specimens (**a**,**c**,**e**) and photomicrographs (**b**,**d**,**f**) of Shimaoshan Group volcanic rocks. Abbreviations: Hbl = Hornblende; Pl = plagioclase; Afs = Alkaline feldspar; Mag = magnetite, Bt = biotite.

3. Analytical Methods

3.1. Zircon U–Pb Dating and Trace-Element Analyses

Conventional density and magnetic methods were used to separate zircon grains from two samples (SH1604, trachyte and ZK5710-30, trachyte), following which grains were hand-picked under a high-resolution optical microscope. Representative zircon grains were set in epoxy resin and then polished to expose their cores. Cathodoluminescence (CL) imaging was used to examine zircon morphology and internal textures and to select analysis locations. Zircon U–Pb dating and trace-element analyses were carried out concurrently by LA–ICP–MS at the State Key Laboratory of Ore Deposit Geochemistry, Institute of Geochemistry, Chinese Academy of Sciences (SKLODG, IGCAS),

Guiyang, China. A GeolasPro 193 nm ArF excimer laser (Coherent, Gilching, Germany) was used to ablate zircons, and an Agilent 7900 ICP–MS instrument (Agilent, Santa Clara, CA, USA) provided ion signal intensities. A mixture of helium and argon was used as the carrier gas to transport the aerosol to the ICP-MS instrument. Zircon 91500 was used as an external standard, and reference materials NIST 610, BIR-1G, BCR-2G, BHVO-2G, PL-1, and QINGHU were used to calibrate the trace-element data. Adopted values of these reference materials are from the GeoReM database [40]. Each sample analysis involved 18 s background acquisition and 50 s data collection. Operating conditions included a laser beam diameter of 32 μm, a repetition rate of 5 Hz, and an energy flux of 8 J/cm^2. ICPMSDataCal software (Version 11.8, Sample Solution, Wuhan, China) was used to process the U–Pb isotopic and trace-element data [41]. Si was used as an internal standard, and multiple elements were used as external standards to calibrate analyzed element contents. Isoplot 4.15 software (Berkeley Geochronology Center, Berkeley, CA, USA) was used to construct concordia plots and calculate weighted mean ages [42].

3.2. Whole-Rock Major- and Trace-Element and Sr–Nd Isotope Geochemical Features

Rock samples were cut into small pieces and fresh parts were selected and ground into powder for whole-rock geochemical analyses. An Axios (PW4400) X-ray fluorescence spectrometer (Thermo Fisher, Waltham, MA, USA) was used to determine contents of major elements at the SKLODG, IGCAS. Loss-on-ignition (LOI) values were measured by heating 1 g sample powder to 1100 °C for 1 h.

Trace-element analyses were also conducted at the SKLODG, IGCAS, by using an ICP–MS instrument (PE DRC-e) produced by PerkinEmer company (Waltham, MA, USA). For each analysis, a 50 mg subsample of rock powder was dissolved at 190 °C in a mixture of HF and HNO_3, and placed in a PTFE-lined stainless-steel bomb for 48 h. To monitor signal drift during counting, Rh was applied as an internal standard. International standards GBPG-1, AGV-2, and AMH-1 were used to monitor analytical quality, with analytical accuracy generally better than ±10%. Details of the experimental procedures followed are given by [43].

A TRITON thermal-ionization mass spectrometer (Thermo Fisher, Waltham, MA, USA) was used to determine Sr–Nd isotope compositions of whole-rock samples at the SKLODG, IGCAS. Samples were dissolved by using the same method as that used for trace elements. Cationic ion-exchange procedures were applied to effectively separate Sr and Nd in solution [44]. Sr and Nd isotopic ratios were normalized with respect to $^{86}Sr/^{88}Sr = 0.1194$ and $^{146}Nd/^{144}Nd = 0.72419$. Details of the experimental method and procedure are given by [45].

3.3. Zircon O Isotope Analyses

Determinations of zircon O isotopic composition were conducted by a Cameca IMS-1280HR secondary-ion mass spectrometer (Camera, Paris, France) at the SIMS laboratory in the Guangzhou Institute of Geochemistry, Chinese Academy of Sciences, Guangzhou, China. Analytical procedures followed those described by [46]. Under conditions of 10 kV and an intensity of ~2 nA, the Cs^+ primary ion beam was accelerated and then rasterized over a 10 μm area. Analysis spots had a diameter of 20 μm. The width of the inlet gap of the multicollector Faraday cup (FC) of ^{16}O and ^{18}O was 120 μm, and the width of the outlet gap was 500 μm. The intensity of ^{16}O was ~1×10^9 counts per second. In multicollector mode, two off-axis Faraday cups were used to measure O isotopes. Each analysis duration included 120 s for pre-sputtering, 60 s for automatic beam formation, and 40 s for O isotope integration. Vienna Standard Mean Ocean Water (VSMOW) composition was used as the standard to normalize $\delta^{18}O$ values. Standard zircon 91500 was used to correct the instrumental mass fractionation factor, with $\delta^{18}O_{VSMOW} = 9.9‰$ [47].

3.4. Zircon Lu–Hf Isotope Analyses

In situ analyses of Hf isotopic compositions of zircon were performed using LA-MC-ICP-MS at the SKLODG, IGCAS. Analyses of Hf were conducted on the same spots as used for O isotope analyses. A RESOlution S-155 LA system (Australian Scientific Instruments, Canberra, Australia) and

a Nu Plasma III MC–ICP–MS instrument (Nu Instruments, Wrexham, Wales, UK) were used together for the analyses. After homogenization of the beam-delivery system, the 193 nm ArF excimer laser was focused on the surface of the zircon with an energy density of 6.0 J/cm^2. Laser ablation involved a spot diameter of 40 μm, a repetition frequency of 6 Hz, and an ablation duration of 40 s. Helium was used as a carrier gas to transport the aerosol to the Nu Plasma III MC-ICP-MS instrument (Nu Instruments, Wrexham, Wales, UK). For quality control, five standard zircons (GJ-1, 91500, Plešovice, Mud Tank, and Penglai) were processed for every 30 unknown analyses, and one standard zircon (Penglai) was processed for every five unknown analyses. The influence of mass deviation on Hf was corrected according to an exponential law by using the value of ^{179}Hf/^{177}Hf = 0.7325 [48]. The isobaric interference of ^{176}Lu on ^{176}Hf was corrected by using the recommended ^{176}Lu/^{175}Lu ratio of 0.02655 [49] to calculate values of ^{176}Lu/^{177}Hf, and the isobaric interference of ^{176}Yb on ^{176}Hf was corrected by using the recommended ^{176}Yb/^{172}Yb ratio of 0.5887 [50] to calculate values of ^{176}Yb/^{177}Hf.

4. Analytical Results

4.1. Zircon U–Pb Dating and Trace Elements

The U–Pb isotope data are listed in Supplementary Table S1, and representative zircon CL images and U–Pb concordia diagrams are shown in Figures 4 and 5, respectively. Zircon crystals from trachyte sample SH1604 are generally euhedral, transparent, and light gray in color, with lengths varying from 100 to 300 μm and aspect ratios from 1:1 to 3:1. The zircon grains have Th and U contents of 205–2127 ppm and 458–1246 ppm, respectively, with Th/U values of ~0.36–1.70 (mostly >0.4), indicating a magmatic origin for these zircons. A total of 18 analyses on 18 zircons from sample SH1604 were obtained after discarding eight ages owing to their high level of discordance, yielding a concordant ^{206}Pb/^{238}U age of 105.04 ± 0.83 Ma (MSWD = 0.03; 1σ), with a weighted mean ^{206}Pb/^{238}U age of 105.12 ± 0.72 Ma (MSWD = 0.03; 1σ). This mean age can be considered as the crystallization age of the trachyte sample. Analysis spots SH1604-10 and SH1604-11 yielded older ^{206}Pb/^{238}U ages of 127.6 and 129.1 Ma, respectively, which we interpret as representing zircons captured from country rock during magma ascent. The features of zircon crystals from trachyte sample ZK5710-30 are similar to those of SH1604 with varying contents of Th and U (150–480 ppm and 421–1655 ppm, respectively) and Th/U values of ~0.29–0.68 (mostly >0.4). A total of 21 analyses on 21 zircons from sample ZK5710-30 were obtained after discarding four ages on account of their high level of discordance, yielding a concordant ^{206}Pb/^{238}U age of 105.08 ± 0.70 Ma (MSWD = 0.02; 1σ), with a weighted mean ^{206}Pb/^{238}U age of 105.08 ± 0.68 Ma (MSWD = 0.02; 1σ). This mean age can be interpreted as the crystallization age of the trachyte sample.

Zircon trace elements are listed in Supplementary Table S1. Zircon Eu_N/Eu_N^* (subscript N = chondrite-normalized) values were calculated, yielding values of 0.48–0.62. The mean value of Dy/Yb is low, about 0.2.

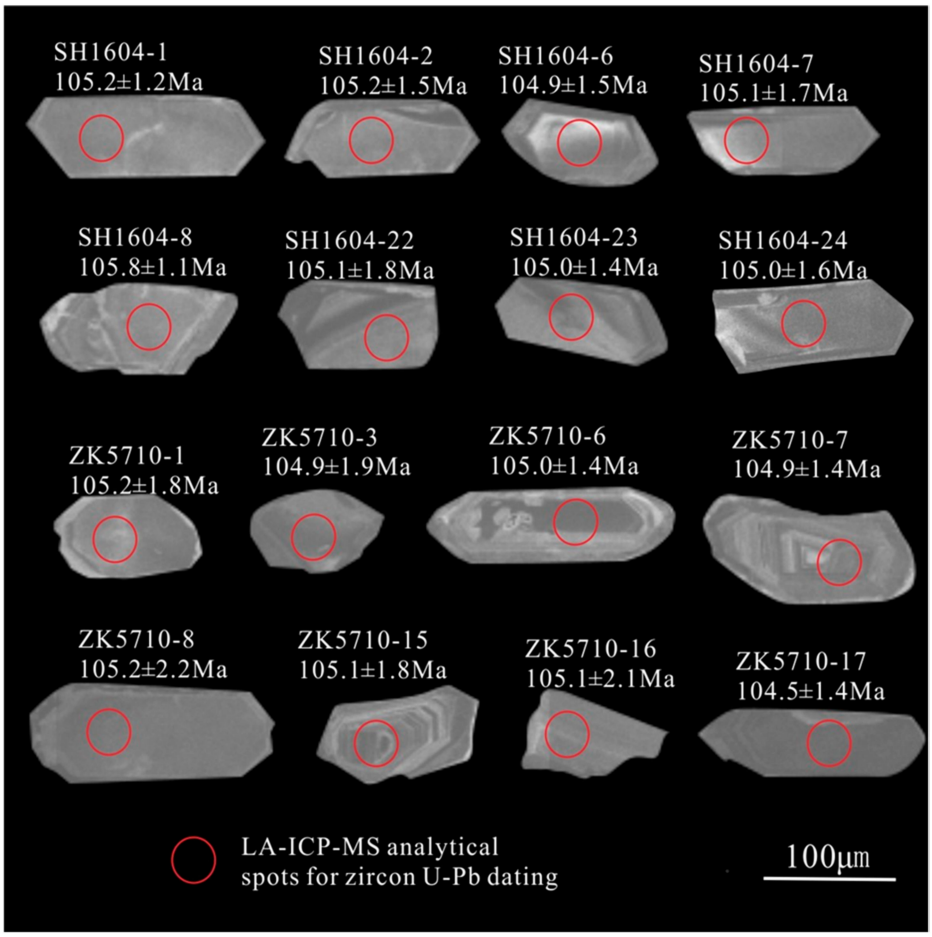

Figure 4. Representative zircon CL images showing internal textures and locations LA-ICP-MS U–Pb dating analysis spots (red circles) of volcanic rocks from the Shanghang Basin.

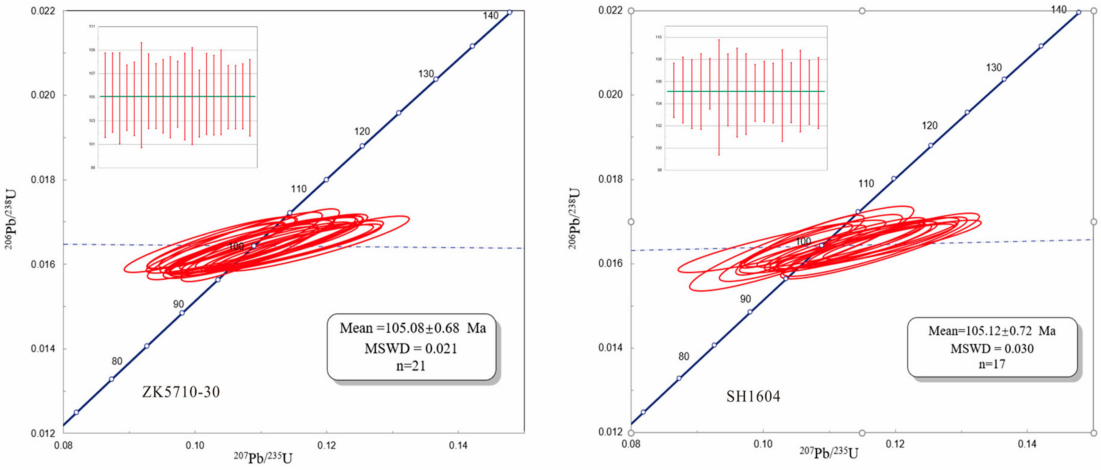

Figure 5. Zircon U–Pb concordia diagrams and weighted mean ages for rock samples SH1604 and ZK5710-30 from the Zijinshan ore district.

4.2. Whole-Rock Major and Trace Elements

Sixty-two volcanic rock samples from the Shanghang Basin were analyzed for major- and trace-element compositions, with results given in Supplementary Table S2. Sample contents were standardized to 100% after accounting for LOI. These samples have SiO_2 contents ranging from 55.40 to 74.82 wt %. Their Na_2O, K_2O, and Na_2O + K_2O contents are 0.10–4.77 wt %, 2.50–12.17 wt %,

and 5.91–12.38 wt %, respectively. On the total-alkali-silica (TAS) diagram, the samples fall mainly in the trachyte and trachydacite, dacite, and trachyandesite fields, with a few plotting in the rhyolite field (Figure 6a), and the samples are classified as high-K calc-alkaline to shoshonitic series (Figure 6b). However, there is no correlation between SiO_2 and K_2O and Na_2O, suggesting the samples experienced variable degrees of post-magmatic alteration. Some samples have high K_2O content and Na_2O content of close to zero, possibly because of the strong alteration, which must be considered when interpreting the data obtained from these rocks. The MgO and TFe_2O_3 contents of the rocks are 0.22–4.91 wt % and 2.13–8.54 wt %, respectively, with $Mg^{\#}$ ($Mg^{2+}/(Fe^{2+} + Mg^{2+})$ in mole ratio) values of 15.1–67.4. The samples have Al_2O_3, CaO, and TiO_2 contents of 12.91–18.62 wt %, 0.12–8.24 wt %, and 0.28–1.43 wt %, respectively. Their molar ratios of A/CNK and A/NK (A/CNK = $Al_2O_3/(CaO + K_2O + Na_2O)$ in mole ratio) are distributed in the metaluminous and peraluminous areas, with a wide range of A/CNK values of 0.66–1.50. With increasing SiO_2 content, contents of $Fe_2O_3{}^T$, Al_2O_3, MgO, TiO_2, Co, and Cr decrease systematically (Figure 7).

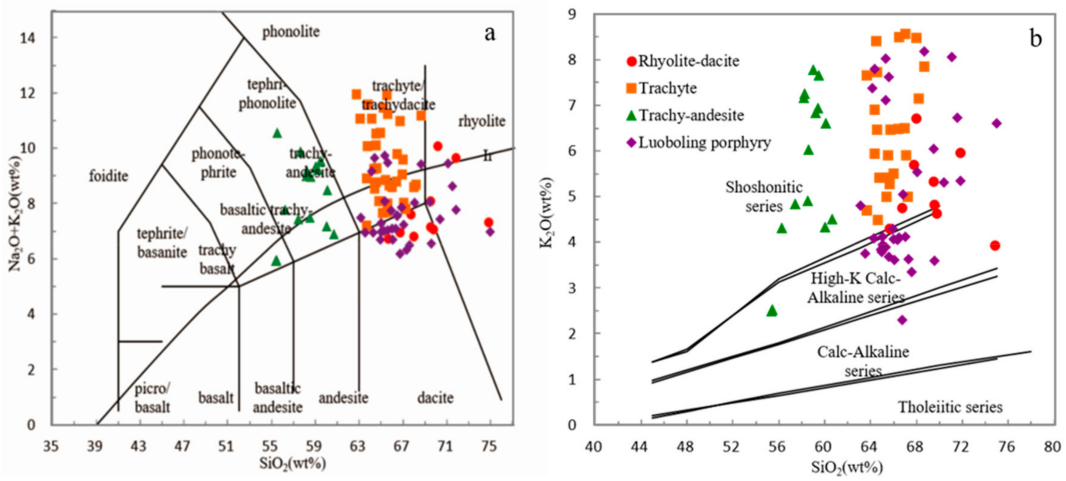

Figure 6. (**a**) Classification of volcanic rocks from the Shanghang Basin by plotting total alkali versus silica (TAS) diagram and (**b**) The whole rock K_2O versus SiO_2 diagram. Data for the Luoboling porphyry are from [32,35,51].

All samples show similar patterns in spider diagrams of trace-element ratios and chondrite-normalized REEs (Figure 8). The samples are characterized by high total REE contents (ΣREE = 115–351 ppm), enrichment in light REEs (LREE) (ΣLREE = 104–327 ppm), steeply inclined REE patterns with strongly fractionated LREEs/HREEs (mean $(La/Yb)_N$ ratio = 16.88), negligible Eu anomalies, enrichment in large-ion lithophile elements (LILEs, such as Rb, Ba, Th, and U), and depletion in high-field-strength elements (HFSEs, such as Nb, Ta, and Ti). The concentrations of some large ion lithophile elements (LILE) such as Rb and Sr are scattered when plotted against with SiO_2, which is attributed to alteration. However, the U contents of these samples are in positive correlation with SiO_2, suggesting that the effect of post-magmatic alteration on U is minimized.

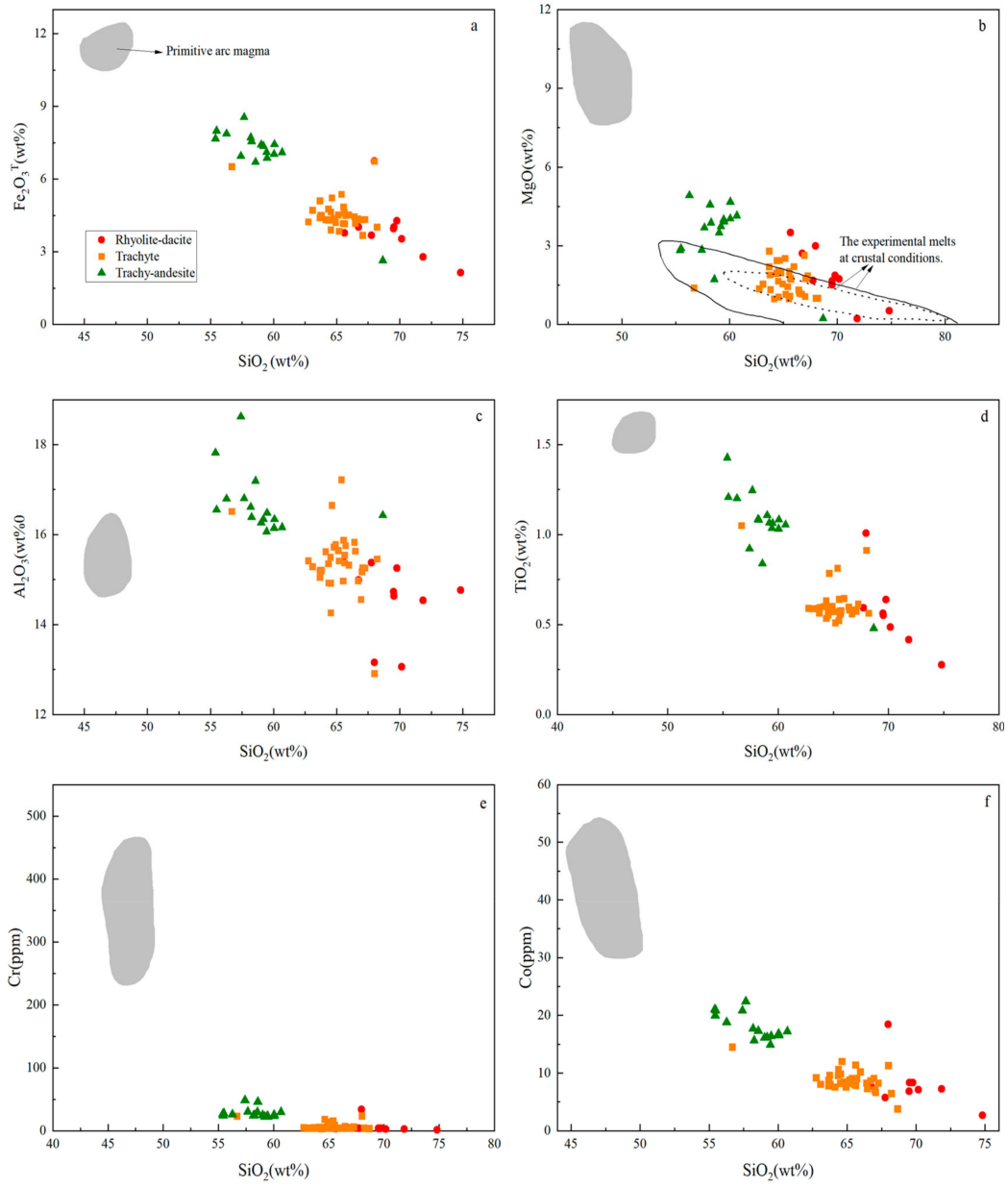

Figure 7. Diagrams of various major oxides and trace elements versus SiO_2 for volcanic rocks from the Shanghang Basin. (**a**) $Fe_2O_3^T$; (**b**) MgO; (**c**) Al_2O_3; (**d**) TiO_2; (**e**) Cr; (**f**) Co. The gray shaded area represents primitive arc melt [52]. The dotted line represents the field of experimental crust melts, data from [36]. the solid line represents the field of metabasaltic and eclogite experimental melts at 1–4 GPa, data from [53].

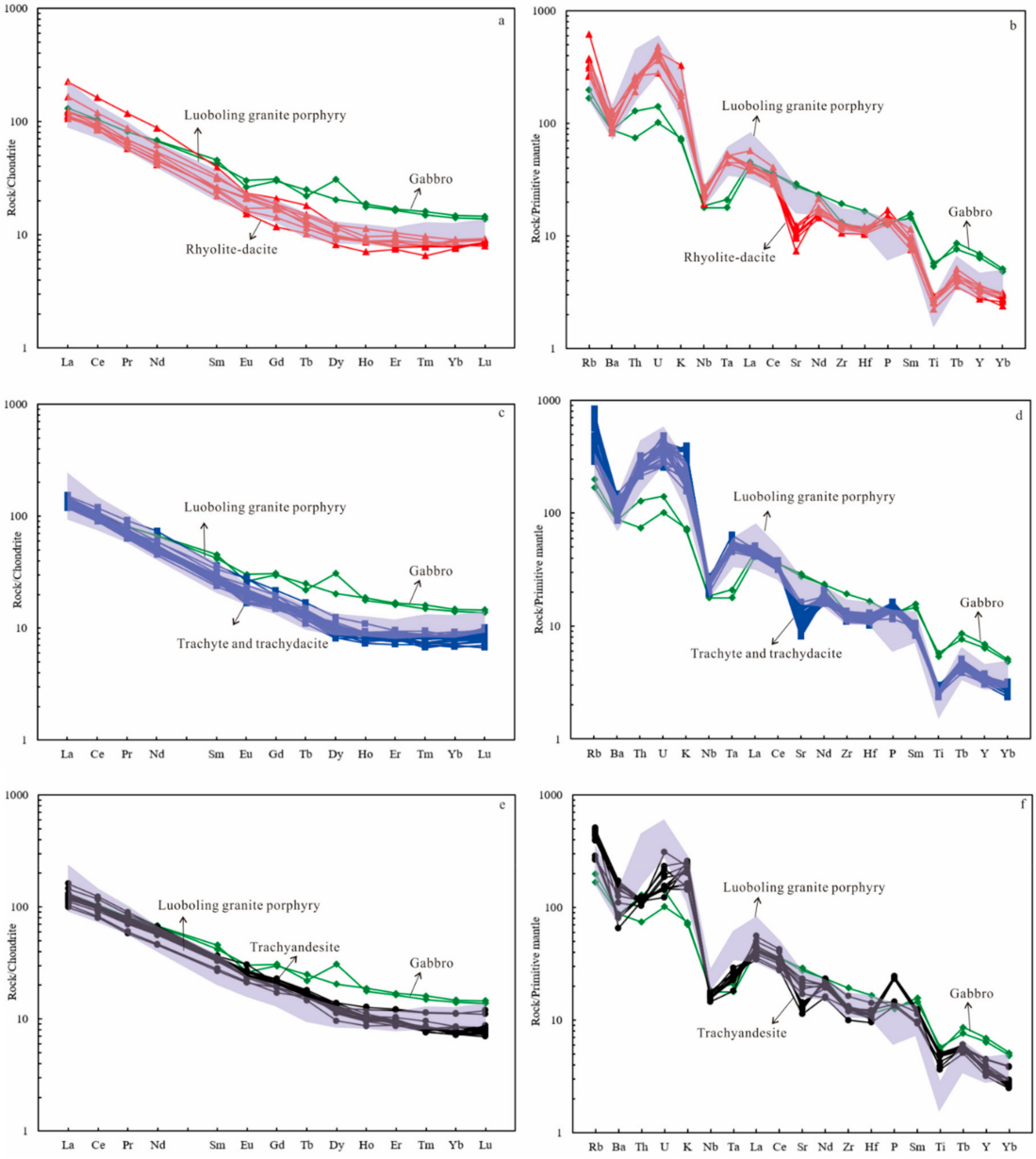

Figure 8. Whole rock Chondrite-normalized rare-earth element (REE) patterns and primitive-mantle-normalized spidergrams for volcanic rocks of the Shimaoshan Group. (**a**,**c**,**e**) The REE patterns of rhyolite-dacite, trachyte and trachydacite, trachyandesite; (**b**,**d**,**f**) The spidergrams of rhyolite-dacite, trachyte and trachydacite, trachyandesite. Normalized values are from [54]. The shaded regions represent the Luoboling granite porphyry, and the green lines represent Cretaceous gabbro from the coastal area of Fujian. Data for the Luoboling granite porphyry are from [32,35,51]; data for gabbro are from [55].

4.3. Whole-Rock Sr–Nd Isotopes

Sr–Nd isotopic compositions of the studied volcanic rocks are presented in Table 1 and Figure 9a. Initial $^{87}Sr/^{86}Sr$ ratios and $\varepsilon_{Nd}(t)$ values were calculated according to the formation age determined by zircon U–Pb dating. The volcanic rocks have $(^{87}Sr/^{86}Sr)_i$ ratios between 0.708901 and 0.711610 and $\varepsilon_{Nd}(t)$ values between −6.9 and −3.3. The higher $(^{87}Sr/^{86}Sr)_i$ values of the volcanic rocks were attributed to post-magmatic alteration, since the Rb and Sr contents of the rocks has been modified by alteration. As a result, the compositions of Sr isotope are excluded in the following discussion.

According to these data, the calculated two-stage depleted-mantle Nd model ages (T_{DM2}) range from 1.47 to 1.19 Ga (Table 1).

Table 1. Rb–Sr and Sm–Nd isotopic data for the volcanic rocks from the Zijinshan ore district.

Rock Type	Rhyolite	Trachyte	Trachyandesite	Trachyandesite	Trachyte
t(Ma)	105	105	105	105	105
Rb($\times10^{-6}$)	207	481	183	282	204
Sr($\times10^{-6}$)	154	235	454	286	297
$^{87}Sr/^{86}Sr$	0.715401	0.720456	0.710641	0.714979	0.712307
$^{87}Rb/^{86}Sr$	3.891373	5.928503	1.166397	2.854424	1.987905
$(^{87}Sr/^{86}Sr)_i$	0.709595	0.711610	0.708901	0.710721	0.709341
Sm($\times10^{-6}$)	4.31	4.25	5.24	5.47	4.1
Nd($\times10^{-6}$)	23.4	22.5	27.6	29.3	23.9
$^{143}Nd/^{144}Nd$	0.512356	0.512373	0.512312	0.512356	0.512404
$^{147}Sm/^{144}Nd$	0.11128	0.11412	0.11470	0.11279	0.10364
$\varepsilon_{Nd}(t)$	−6.9	−4.1	−5.3	−4.4	−3.3
T_{DM2}(Ga)	1.47	1.24	1.33	1.26	1.19

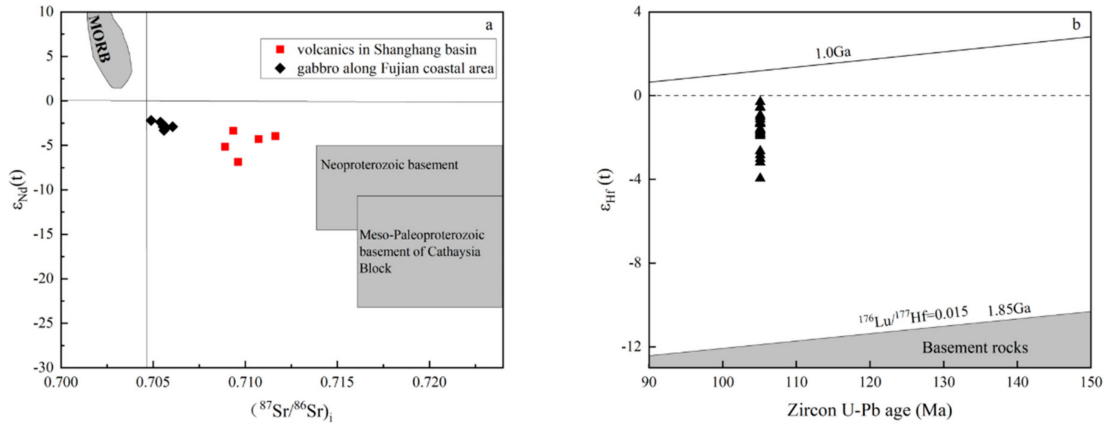

Figure 9. (**a**) Whole rock $\varepsilon_{Nd}(t)$ versus $(^{87}Sr/^{86}Sr)_i$ diagram for the volcanic rocks from the Shanghang Basin. The fields are from [56,57]. Data for Cretaceous gabbro from the coastal area in Fujian are from [55]. (**b**) Zircon $\varepsilon_{Hf}(t)$ versus U–Pb age diagram for the volcanic rocks from the Shanghang Basin. The gray field represents Cathaysia basement rocks, data are from [25,58].

4.4. In Situ Zircon Hf–O Isotopes

One sample (ZK5710-30) was selected for analysis of zircon Hf–O isotopes, due to their high magmatic zircon content. Results are presented in Table 2 and Figure 9b. The $\varepsilon_{Hf}(t)$ value and the two-stage depleted mantle Hf model age were calculated according to the age obtained by zircon U–Pb dating. Twenty-one analyses for sample ZK5710-30 yielded $^{176}Hf/^{177}Hf$ ratios between 0.282597 and 0.282701, and the calculated $\varepsilon_{Hf}(t)$ values range from −3.95 to −0.30, corresponding to two-stage Hf model ages of 1.47 to 1.19 Ga. Fifteen O isotope analyses were obtained with $\delta^{18}O$ values ranging from 6.07‰ to 6.79‰, which are higher than the mantle value of 5.3‰ ± 0.3‰ (Figure 10).

Table 2. Hf-O isotopic data for the volcanic rocks from the Zijinshan ore district.

Spots	t(Ma)	$^{176}Lu/^{177}Hf$	2σ	$^{176}Hf/^{177}Hf$	2σ	$\varepsilon_{Hf}(t)$	2σ	T_{DM2}(Ga)	$f_{Lu/Hf}$	$\delta^{18}O$(‰)	2σ
ZK5710-30											
01	105.2	0.001209	0.000009	0.282701	0.000013	−0.30	0.46	1.18	−0.96	6.64	0.19
02	105.4	0.001487	0.000031	0.282672	0.000011	−1.32	0.39	1.25	−0.96	6.79	0.15
03	105.0	0.000700	0.000004	0.282680	0.000013	−1.02	0.46	1.23	−0.98	6.25	0.17
05	104.5	0.001004	0.000004	0.282661	0.000012	−1.72	0.42	1.27	−0.97	6.47	0.16
06	105.0	0.000937	0.000003	0.282680	0.000013	−1.02	0.46	1.23	−0.97	6.37	0.14
07	104.9	0.000942	0.000007	0.282662	0.000012	−1.64	0.42	1.27	−0.97	6.65	0.20
08	105.2	0.000962	0.000008	0.282692	0.000013	−0.58	0.46	1.20	−0.97	6.26	0.18
09	105.5	0.004121	0.000110	0.282629	0.000011	−3.02	0.39	1.35	−0.88	6.23	0.18
10	105.1	0.000960	0.000008	0.282673	0.000013	−1.28	0.46	1.24	−0.97	6.66	0.23
11	105.0	0.000842	0.000006	0.282628	0.000013	−2.84	0.46	1.34	−0.97	6.43	0.20
12	105.1	0.000772	0.000006	0.282657	0.000014	−1.80	0.50	1.28	−0.98	6.44	0.19
13	105.0	0.001154	0.000008	0.282671	0.000013	−1.35	0.46	1.25	−0.97	6.11	0.17
14	105.3	0.001121	0.000006	0.282673	0.000013	−1.28	0.46	1.24	−0.97	6.17	0.20
15	105.1	0.001119	0.000009	0.282619	0.000012	−3.18	0.42	1.36	−0.97	6.07	0.16
16	105.1	0.000795	0.000007	0.282664	0.000013	−1.58	0.46	1.26	−0.98		
17	104.5	0.002609	0.000048	0.282680	0.000010	−1.13	0.35	1.23	−0.92		
18	105.3	0.001138	0.000006	0.282634	0.000013	−2.64	0.46	1.33	−0.97		
19	105.2	0.000784	0.000006	0.282660	0.000012	−1.70	0.42	1.27	−0.98		
20	105.4	0.000817	0.000005	0.282682	0.000012	−0.93	0.42	1.22	−0.98		
21	105.0	0.001096	0.000008	0.282597	0.000012	−3.95	0.42	1.41	−0.97		
22	105.0	0.001515	0.000026	0.282656	0.000012	−1.92	0.42	1.28	−0.97		
24	105.1	0.001274	0.000009	0.282694	0.000012	−0.54	0.42	1.20	−0.96		
25	105.0	0.000669	0.000002	0.282656	0.000013	−1.83	0.46	1.28	−0.98		

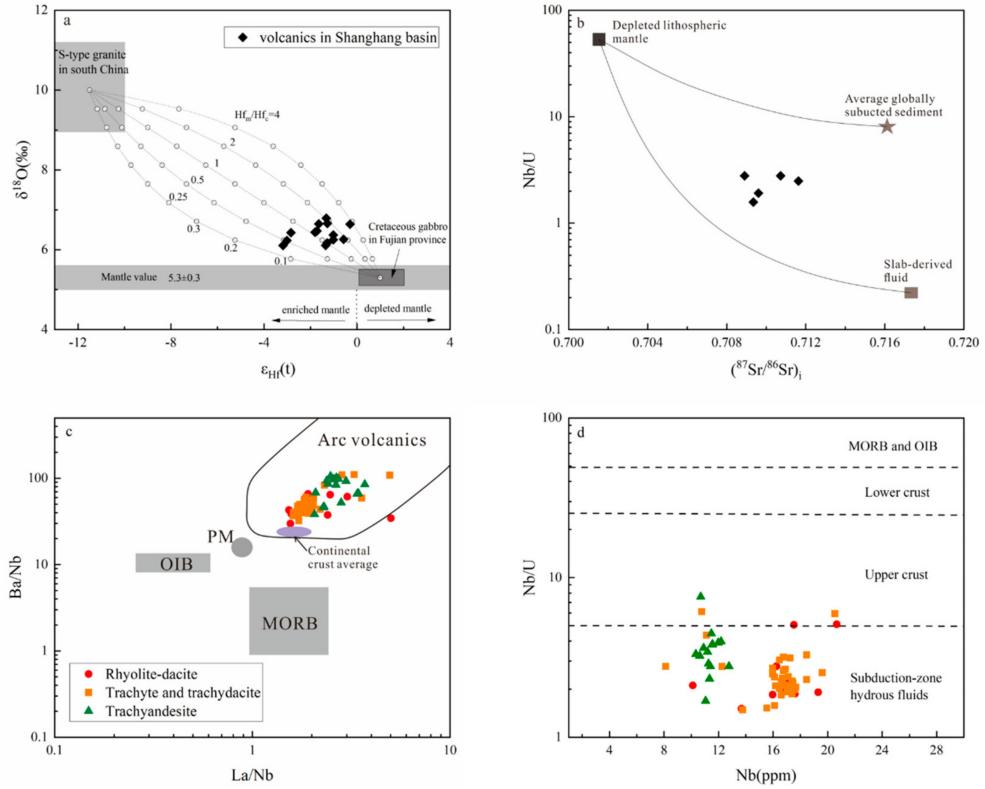

Figure 10. Element and isotope variation diagrams for volcanic rocks from the Shanghang Basin. (**a**) Zircon $\delta^{18}O$ versus $\varepsilon_{Hf}(t)$. The S-type granite compositions are $\varepsilon_{Hf}(t)$ = –12 and $\delta^{18}O$ = 10‰. The Fujian Cretaceous gabbro compositions are $\varepsilon_{Hf}(t)$ = 1 and $\delta^{18}O$ = 5.3‰. Data for S-type granite in South China and Fujian Cretaceous gabbro are from [55,59,60],; (**b**) The whole rock Nb/U versus $(^{87}Sr/^{86}Sr)_i$. Data for globally subducted sediment and slab-derived fluid are from [61,62]; (**c**) The whole rock Ba/Nb versus La/Nb. Data for arc volcanic rocks, average continental crust, OIB, PM, and MORB are from [63]; (**d**) The whole rock Nb/U versus Nb. The regions between the dashed lines are from [64–66].

5. Discussion

5.1. Timing of Volcanism and Relationship to Porphyry-Epithermal Mineralization

In the Zijinshan porphyry-epithermal metallogenic system, the direct ore-forming magma of the epithermal deposits has not been discovered. However, Shimaoshan Group volcanic rocks are distributed extensively in and around the ore district (Figure 2). Understanding the relationship of the volcanism in the Shanghang Basin to porphyry-epithermal mineralization at Zijinshan can help to understand the nature of the metallogenic magma source area and the controls on metallogenesis. Our zircon U–Pb dating results show that volcanism in the Shanghang Basin occurred at ~105 Ma, synchronous with the metallogenic age of the Zijinshan Cu–Au deposit (103 ± 1 Ma, [67]) and the Luoboling porphyry Cu–Mo deposit (104.9 ± 1.6 Ma, [2]; 104.6 ± 1.0, [5]). The Luoboling granodiorite porphyry and the studied volcanic rock samples partially overlap in the K_2O vs. SiO_2 diagram, mainly in the trachyte-dacite-rhyolite field (Figure 6a). However, the volcanic rocks have a wider range of SiO_2 (55–75 wt %), and the Luoboling porphyry are all acidic (63–73 wt %) (Figure 6a), indicating that the magma that formed the porphyry underwent a higher degree of evolution relative to that of the volcanic rocks. Both the studied volcanic rocks and the Luoboling porphyry belong to the high-K calc-alkaline and shoshonitic series in a $Na_2O + K_2O$ vs. SiO_2 diagram (Figure 6b). Moreover, the volcanic rocks have similar REE and trace-element patterns to those of the Luoboling porphyry (Figure 8). These features, together with the similar ages and the close temporal and spatial relationships between the volcanic rocks and porphyries, indicate that the volcanic rocks and the magma were derived from a common magma chamber beneath the volcanic basin and underwent similar fractionation pathways.

5.2. Magma Source of the Volcanic Rocks

The Shimaoshan Group volcanic rocks in the Shanghang Basin show high MgO contents and high $Mg^{\#}$ values relative to those of experimental crustal melt (Figure 7b), suggesting that the volcanic magmas cannot have originated from partial melting of crustal materials. The two-stage Hf model ages of 1.41 to 1.18 Ga (Table 2) are substantially younger than those of basement metamorphic rocks of the Cathaysia Block (>1.85 Ga, [25]) (Figure 9b), indicating that the crust was not the only source of the volcanic rocks. In addition, the Sr–Nd isotope data of the studied samples differ substantially from those of Neoproterozoic and Meso-Paleoproterozoic basement rocks of the Cathaysia Block (Figure 9a), with two-stage Nd model ages of 1.47 to 1.19 Ga (Table 1) that are much younger than those of basement metamorphic rocks of the Cathaysia Block (>1.74 Ga, [68]). Experimental studies on melting have shown that continental crust melts are usually sodium rich [69,70], but our samples are high-K calc-alkaline and shoshonitic. Therefore, Shimaoshan Group volcanic rocks were not derived from a predominant crustal source.

The enriched Sr–Nd–Hf isotopic features of the samples, together with the older Hf and Nd model ages (1.47–1.19 Ga), indicate that the parental melts of the studied volcanic rocks were derived from enriched mantle or a mixture of mantle-derived magma and crust-derived magma. Nb/Ta values can serve as an important indicator of crust–mantle interaction [71]. Continental crust has an average Nb/Ta ratio of 11.43 [62] and primitive mantle of 17.8 [72]. The Shanghang Basin volcanic rocks show Nb/Ta ratios that range from 7.03 to 18.18, with a mean value of 10.11, which is near the value of average continental crust. The low Nb/Ta ratios cannot fully interpret as the result of crustal contamination, since an unreasonable proportion of crustal materials is required to cause such a low ratio. All the Cretaceous mafic plutons in the Fujian coastal area of southeastern China have a narrow range of negative $\varepsilon_{Nd}(t)$ values (−1.3 to −3.3; [73]). This, together with the mantle-like $\delta^{18}O$ value of these mafic plutons [55] indicates that these rocks reflect the characteristics of a mantle source and that crustal assimilation was negligible during magma ascent. However, the volcanic rocks are more enriched in Sr–Nd compared with the mafic plutons, consistent with minor crustal contamination of the parental magma.

Zircon O isotopes can effectively distinguish crustal contamination [74] because mantle-derived magma and upper-crust-derived magma have distinct O isotope characteristics, with $\delta^{18}O$ values of 5.3‰ and 10‰–30‰, respectively [75]. $\delta^{18}O$ values of our samples vary from 6.07‰ to 6.79‰ (Table 2) and are much higher than the mantle $\delta^{18}O$ range (Figure 10a). This, combined with the negative correlation between zircon $\delta^{18}O$ and $\varepsilon_{Hf}(t)$, indicates that the volcanic rocks in the Shanghang Basin were derived from enriched mantle but also affected by some crustal contamination. We performed quantitative modeling on the basis of the zircon $\delta^{18}O$ and $\varepsilon_{Hf}(t)$ isotopic compositions by magma mixing of two end members to estimate the degree of crustal contamination. The Cretaceous gabbro near the study area and South China S-type granite were selected as the two end members, representing the mantle and crust components, respectively. The final composition of the mixture depends on the ratio of the two end members, each curve represents a mixed case, and the curvature of the curve is controlled by Hf_m/Hf_c. The results indicate that the degree of crustal contamination is <30% (Figure 10a).

The samples show strong fractionation between LREEs and HREEs, enrichment of LILEs, and depletion in HFSEs, with negative Nb–Ta and Ti anomalies (Figure 8d–f). These characteristics are consistent with those of non-crust-contaminated Cretaceous mafic suites in the Cathaysia Block [55,76]. Slab-derived fluids or subducted sediments can enrich mantle sources, giving rise to enrichment in LILEs and depletion in Nb, Ta, and Ti [77], consistent with our results (Figure 10b). The studied volcanic samples have very similar Nd isotope characteristics to those of the Cretaceous gabbro in the Fujian coastal area (Figure 9a) [55], further suggesting a similar mantle derivation with the gabbro. Moreover, their high La/Nb and Ba/Nb ratios are consistent with the characteristics of arc volcanic rocks (Figure 10c), which are generally considered to be related to subduction [78]. In addition to the above indicators, the ratios of incompatible trace elements with similar distribution coefficients, such as Nb/U, Nb/Ta, and Ce/Pb, can also be used to distinguish the source region, as they show negligible change during the melting process [79,80]. The Nb/U values (1.49–7.58) of the studied samples are much lower than those of MORB and OIB (Figure 10d), indicating that these rocks were metasomatized by subduction-related hydrous fluids. Thus, we suggest that these volcanic rocks were derived from mantle material enriched by input of subduction-related materials.

The extensive magmatic activity during the Cretaceous in the Cathaysian Block is generally considered to have been the result of westward subduction of the Paleo-Pacific Plate [10,81], which could account for the inferred enrichment of mantle material. The Zijinshan ore district volcanic rocks share similar REE and trace-element patterns and Sr–Nd–Hf isotope characteristics with typical arc volcanic rocks, suggesting a subduction affinity. In addition, the volcanic rocks represent high-K calc-alkaline to shoshonitic lavas, which are different from the intermediate, low-K to calc-alkaline rocks in modern arc environments [82]. High-K, calc-alkaline to shoshonitic rocks are also found in lithospheric extensional settings [83]. Accordingly, the characteristics and age of volcanic rocks of the Shimaoshan Group suggest that the coastal region of southeastern China was situated in a lithospheric extensional setting during the Cretaceous. It has been proposed that the regional tectono-magmatic evolution in southeastern China during the late Yanshanian was controlled by break-off and rollback of the subducting paleo-Pacific Plate [73]. Thus, we suggest that this geodynamic process caused regional extension and partial melting of the mantle lithosphere in the Zijinshan district and the Shanghang Basin to produce magmas that ultimately formed the volcanic rocks.

5.3. Petrogenesis

The SiO_2 contents of melts directly produced by partial melting of mantle material are less than 57 wt % [84,85]. However, the SiO_2 contents of the studied Shimaoshan Group volcanic rocks range from 56 to 71 wt %, suggesting that these rocks do not represent the primary magma derived from partial melting of the mantle. Similarly, the $Mg^{\#}$ values of primitive arc melts are generally >70 [86], compared with <67 (most <50) of the studied rocks, meaning that these volcanic rocks were formed from mantle-derived magma after a high degree of fractional crystallization in a deep magma

chamber [87]. This interpretation is supported by the lower contents of some compatible elements in the volcanic rocks. For example, the Cr (1.2–48.3 ppm) and Ni (1.8–35.6 ppm) contents of the samples are considerably lower than those of primitive arc magma (Cr = 364 ppm, Ni = 168 ppm) [88] (Figure 7). Given that Cr tends to enter Cr-spinel and clinopyroxene, and Ni generally enters olivine, fractional crystallization of olivine, clinopyroxene, and Cr-spinel is inferred to have occurred during the early stage of magma evolution. Moreover, the volcanic rocks are not depleted in Al_2O_3 content relative to primitive arc magma (Figure 7c), suggesting that plagioclase crystallization was negligible in the early stage of magma differentiation. In addition, there is no negative Eu anomaly apparent in an REE variation diagram (Figure 8a,c,e), also indicating that early fractional crystallization of plagioclase was negligible.

The SiO_2 content of the studied samples is negatively correlated with various elements, including $Fe_2O_3{}^T$, MgO, Al_2O_3, and TiO_2 (Figure 7). These negative correlations can be interpreted in terms of fractionation of mafic minerals, such as magnetite, hornblende, and biotite, which tend to remove most of the Fe, Mg, and Ca from melts and cause them to evolve toward more silicic compositions [4]. Owing to different partition coefficients of the various elements, a correlation diagram of the element ratios can qualitatively determine separation of mineral phases. For example, fractionation of biotite can lead to an increase in SiO_2/Al_2O_3 and a decrease in Sc/Th (Figure 11a), and fractionation of hornblende can result in a positive correlation between Dy/Yb and Nb/Ta (Figure 11b). These patterns suggest that the magma underwent fractional crystallization of amphibole and biotite when it evolved from an andesitic to a dacitic composition. The observed decreases in V and Ti with SiO_2 may be related to the separation of Fe–Ti oxides, such as magnetite, as supported by microscope observations (Figure 3f). Moreover, fractional crystallization and partial melting trends can be distinguished in diagrams of Ni versus Rb and Ni versus Ba (Figure 11c,d).

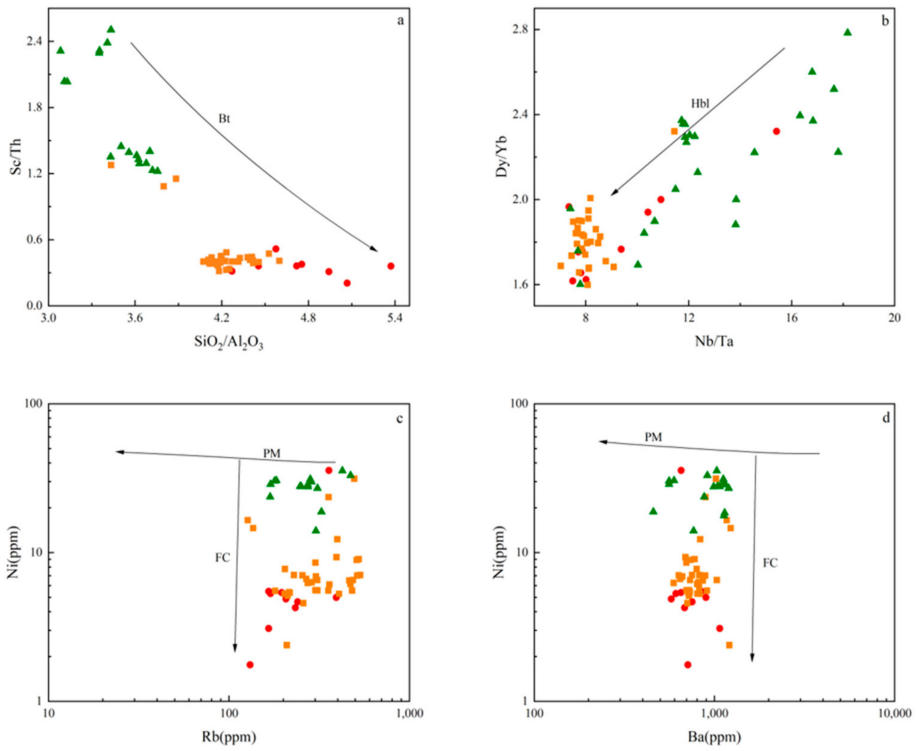

Figure 11. Whole rock element variation diagrams for volcanic rocks from the Shanghang Basin. (**a**) Sc/Th versus SiO_2/Al_2O_3; (**b**) Dy/Yb versus Nb/Ta; (**c**) Rb (incompatible element) versus Ni (compatible element); (**d**) Ba (incompatible element) versus Ni (compatible element). The symbols are the same as in Figure 7. PM: Partial melting; FC: Fractional crystallization.

In summary, the parental magma underwent fractional crystallization of Cr-spinel and clinopyroxene in the deep magma chamber with suppression of plagioclase crystallization. During magma ascent, biotite and hornblende were the main mineral phases. After mineral separation, the magma was emplaced at shallow or surficial crustal levels, forming the Shimaoshan Group volcanic rocks in the Zijinshan district.

5.4. Implications for Porphyry-Epithermal Mineralization

The water content and oxygen fugacity of the magma are the most important controls on the metallogenic potential of porphyry magmas [89–91]. In a comagmatic system, important physical–chemical information of the parental magmas can be obtained from volcanic rocks [90,92]. In turn, the fO_2–H_2O conditions in the parental magma of volcanic rocks provide insights into the metallogenic potential of the porphyries in the Zijinshan ore district.

It is difficult to evaluate the original magmatic oxidation state in altered plutonic rocks, but normalized zircon Ce and Eu anomalies of volcanic rocks can be used to provide qualitative estimations [89,93,94]. The element Eu has two valence states: Eu^{3+} and Eu^{2+}. Eu^{3+} is a more compatible ion than Eu^{2+} and can therefore more readily replace zirconium ions in the zircon crystal lattice, but it requires more oxidizing conditions. Thus, the ratio Eu_N/Eu_N^* can be used as a suggestion of magma oxygen fugacity [89,95]. To avoid the influence of mineral inclusions (such as apatite and titanite), we used Ca > 200 ppm or La > 0.3 ppm as an indicator of apatite contamination and Ti > 20 ppm to reflect titanite contamination [96]. At the same time, plagioclase crystallization would also influence on Eu_N/Eu_N^*. As a result, samples with similar SiO_2 content (63–66 wt %) were selected for comparison, which represented that they have similar degrees of differentiation. Zircon Eu_N/Eu_N^* values of the volcanic rocks are similar to those the Luoboling porphyry deposit and to some other porphyry deposits in the world [89,96,97] (Figure 12a), suggesting that the parental magma was of high oxygen fugacity. In a diagram of $Fe_2O_3^T$ versus MgO (Figure 12b), $Fe_2O_3^T$ content is positively correlated with MgO content for the studied rocks, with the change in slope marking magnetite saturation, indicating that magnetite had crystallized and separated from the magma. The onset of magnetite saturation from basaltic magma is controlled largely by oxygen fugacity [98]. As shown in Figure 12b, the onset of magnetite saturation in the parental magma of the volcanic rocks was like that in other typical arc magmas worldwide. This early saturation of magnetite suggests that the oxygen fugacity of magma that formed the studied Shimaoshan Group volcanic rocks was relatively high.

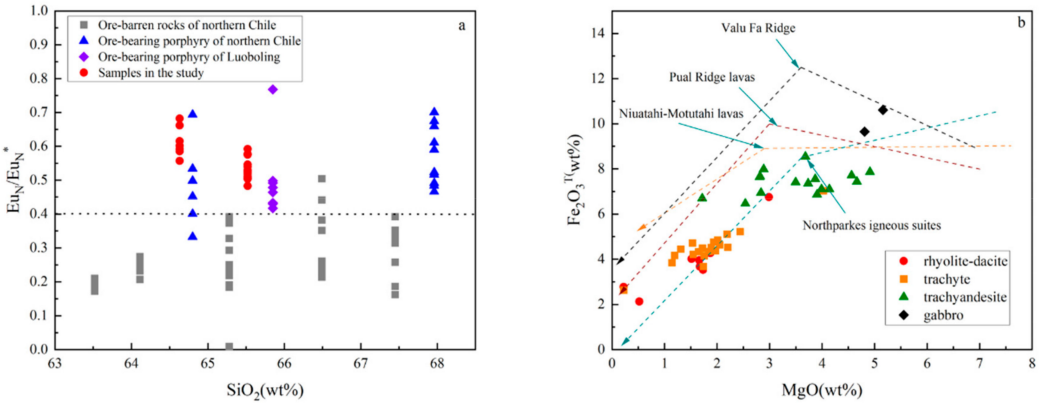

Figure 12. (**a**) Zircon Eu_N/Eu_N^* versus whole rock SiO_2 for volcanic rocks from the Shanghang Basin and other porphyry deposits (data for other deposits are from [4,35,51,89]). (**b**) Whole rock $Fe_2O_3^T$ versus MgO for volcanic rocks from the Shanghang Basin and other arc magmas, data for the latter are from [99–102].

Previous studies have shown that water-rich magma is liable to dissolve volatiles during its evolution, which is conducive to enrichment and migration of ore-forming elements [103]. A high-water

content of the magma inhibits early crystallization of plagioclase and promotes crystallization of amphibole, which can generate some trace element anomalies. For example, the magma has a higher Sr content when crystallization of plagioclase is inhibited, because there is very little Sr to replace Ca into plagioclase lattice. At the same time, medium REEs and Y can readily enter amphibole in intermediate to acidic magma, and the crystallization of amphibole in water-rich magma reduces its Y content. Therefore, water-rich magma commonly shows a high whole-rock Sr/Y ratio [104,105], consistent with our results (Sr/Y = 4.4–54.6, mostly >20), which suggest separation of amphibole. REE patterns also suggest that these elements entered amphibole during the crystallization process (Figure 8a,c,e) [96]. In addition, our samples have a whole-rock mean $[La/Sm]_N$ value of 4.53, much higher than that of Zijinshan barren rocks (3.8, [35]), and have low mean Dy/Yb values of 0.2 in the zircon and high whole-rock V/Sc ratios (mean = 9.12), indicating a high water content of the magma [91,94]. Furthermore, Eu^{2+} can easily replace Ca^{2+} in plagioclase, meaning that the Eu anomaly can be used to indicate the crystallization of plagioclase: a strong negative anomaly indicates early crystallization of plagioclase; and a weak negative anomaly suggests either that the magma had a high water content that inhibited crystallization of plagioclase or that the magma had a high oxygen fugacity with Eu existing mainly as Eu^{3+}. Chondrite-normalized REE patterns (Figure 8) show either a weak negative or negligible Eu anomaly (Eu_N/Eu_N^* = 0.89–1.06), suggesting that fractional crystallization of plagioclase can be ignored.

High oxygen fugacity can facilitate porphyry mineralization in multiple stages of magmatic evolution [106]. In addition, high water contents of ore-forming magma are a key control on the formation of porphyry deposits [107,108]. Copper, gold, and molybdenum are all chalcophile elements with high partition coefficients between sulfides and melts, with the behaviors of Cu and Au being strongly controlled by sulfides [109]. Oxygen fugacity controls sulfur speciation, which in turn is the dominant influence on S solubility of natural silicate melts [110]. The solubility of sulfate is one order of magnitude higher than that of sulfide [110]. Under conditions of high oxygen fugacity, most of the sulfur is removed in the form of sulfate during partial melting of a mantle source [110], leading to the release of abundant chalcophile-forming metals from the magma [111]. In contrast, sulfide saturation in the magma is suppressed by the high solubility of sulfur, resulting in chalcophile-forming metals (e.g., Cu and Au) being retained in the magma [112]. Moreover, high oxygen fugacity favors the presence of Mo as MoO_4^{2-}, which promotes enrichment of Mo in residual melt [113]. Water-rich magma is more likely to reach water saturation, which is conducive to the extraction and dissolution of volatiles. These volatiles are readily combined with gold, copper, and other ore-forming elements to form soluble complexes, which facilitates the enrichment and migration of ore-forming elements. Combining all of the above, we conclude that the high water content and high oxygen fugacity of the source magma promoted mineralization of the Zijinshan epithermal–porphyry deposit system.

6. Conclusions

(1) Zircon U–Pb isotope dating yielded an age of 105 Ma for the Shimaoshan Group volcanic rocks, which is identical to the mineralization age of the nearby porphyry-epithermal ore deposits in the Zijinshan district. This, together with the similar geochemical features, suggests that the volcanic rocks and the mineralization were derived from magmas residing in a common magma chamber beneath the volcanic basin and that these magmas underwent similar fractionation pathways.

(2) Major- and trace-element geochemistry reveals that the volcanic rocks from the Shanghang Basin are predominantly high-K and shoshonitic rocks. Sr–Nd–Hf and O isotopes of the rocks indicate that they were derived predominantly from partial melting of the subduction-modified mantle in a back-arc extension setting as a response to rollback of the subducting paleo-Pacific Plate. Extensive fractional crystallization and crustal contamination account for the compositional variation in the volcanic rocks.

(3) High Eu_N/Eu_N^* values of the studied volcanic rocks and the inferred early crystallization of magnetite imply a high oxygen fugacity of the parental magma. Inferred hornblende crystallization

and inhibition of plagioclase crystallization indicate a high-water content of the magma. High oxygen fugacity and high-water content promoted the dissolution of Cu- and Au-bearing sulfides in the source area and the concentrating of Cu and Au in the magma to form metal- and water-rich magma, followed by extraction of these elements from the magma by volatiles. We conclude that the high oxygen fugacity and high water content were important controlling factors in the formation of the Zijinshan ore deposit.

Supplementary Materials: The following are available online at http://www.mdpi.com/2075-163X/10/2/200/s1. Supplementary Table S1: Zircon U-Pb dating results and zircon trace elements obtained by LA-ICP-MS of the volcanic rocks from Zijinshan ore district; Supplementary Table S2: Whole rock major and trace elements analysis results of the volcanic rocks from Zijinshan ore district.

Author Contributions: Conceptualization, Z.-Z.F. and Z.-J.B.; methodology, Z.-Z.F. and Z.-J.B.; article writing and figure drawing, Z.-Z.F.; project administration, H.Z.; supervision, W.-G.Z. and H.Z.; sample collection, S.-J.Z. Funding acquisition, Z.-J.B. and H.Z. All authors have read and agreed to the published version of the manuscript.

Funding: This study was financially supported by the National Key R&D Program of China (2016YFC0600405) and National Natural Science Foundation of China (41425011, 41873055).

Conflicts of Interest: The authors declare no conflict of interest.

References

1. Zhang, J.Z. Geology, exploration model and practice of Zijinshan ore concentrated area. *Miner. Depos.* **2013**, *32*, 757–766. (In Chinese)
2. Liang, Q.L.; Jiang, S.H.; Wang, S.H.; Li, C. Re-Os dating of the molybdenite from the Luobuling porphyry copper-molybdenum deposit and its geological significance in the Zijinshan orefield, Fujian. *Acta Geol. Sin.* **2012**, *86*, 1113–1118. (In Chinese)
3. Wu, L.Y.; Hu, R.Z.; Qi, Y.Q.; Zhu, J.J. Zircon LA-ICP-MS U-Pb ages and geochemical characteristics of quartz syenite porphyry from Jintonghu deposit in Zijinshan ore field, Fujian Province, South China. *Acta Pet. Sin.* **2013**, *29*, 4151–4166. (In Chinese)
4. Li, B.; Jiang, S.Y. Geochronology and geochemistry of Cretaceous Nanshanping alkaline rocks from the Zijinshan district in Fujian Province, South China: Implications for crust–mantle interaction and lithospheric extension. *J. Asian Earth Sci.* **2014**, *93*, 253–274. [CrossRef]
5. Zhong, J.; Chen, Y.J.; Pirajno, F.; Chen, J.; Li, J.; Qi, J.P.; Li, N. Geology, geochronology, fluid inclusion and H–O isotope geochemistry of the Luoboling Porphyry Cu–Mo deposit, Zijinshan Orefield, Fujian Province, China. *Ore Geol. Rev.* **2014**, *57*, 61–77. [CrossRef]
6. Hua, R.M.; Lu, J.J.; Chen, P.R.; Li, X.F.; Liu, X.D.; Zhang, W.L. The late Mesozic porphyry-epithermal Au-Cusystem in east China and their ore-forming fluieds. *Prog. Nat. Sci.* **2002**, *12*, 240–244. (In Chinese)
7. Zhang, D.Q.; She, H.Q.; Li, D.X.; Feng, C.Y. The porphyry-epithermal metallogenic system in the Zijinshan region, Fujian Province. *Acta Geol. Sin.* **2003**, *77*, 253–261. (In Chinese)
8. Zhang, D.Q.; Feng, C.Y.; Li, D.X.; She, H.Q.; and Dong, Y.J. The Evolution of Ore-forming Fluids in the Porphyry-Epithermal Metallogenic System of Zijinshan Area. *Acta Geos. Sin.* **2005**, *26*, 127–136. (In Chinese)
9. Huang, R.S. Igneous rock series and epithermal-porphyry copper gold and silver mineralization system in Fujian Zijinshan ore field. *J. Geomech.* **2008**, *14*, 74–86. (In Chinese)
10. Zhou, X.M.; Sun, T.; Shen, W.Z.; Shu, L.S.; Niu, Y.L. Petrogenesis of Mesozoic granitoids and volcanic rocks in South China: A response to tectonic evolution. *Episodes* **2006**, *29*, 26–33. [CrossRef]
11. Li, X.Y.; Li, S.Z.; Suo, Y.H.; Dai, L.M.; Guo, L.L.; Ge, F.J.; Lin, P.J. Late Cretaceous basalts and rhyolites from Shimaoshan Group in eastern Fujian Province, SE China: Age, petrogenesis, and tectonic implications. *Int. Geol. Rev.* **2017**, *60*, 1721–1743. [CrossRef]
12. So, C.S.; Zhang, D.Q.; Yun, S.T.; Li, D.X. Alteration-mineralization zoning and fluid inclusions of the high sulfidation epithermal Cu-Au mineralization at Zijinshan, Fujian Province, China. *Econ. Geol.* **1998**, *93*, 961–980. [CrossRef]
13. Zhong, J.; Chen, Y.J.; Chen, J.; Li, J.; Qi, J.P.; Dai, M.C. Fluid inclusion study of the Luoboling porphyry Cu-Mo deposit in the Zijinshan orefield, Fujian Province. *Acta Pet. Sin.* **2011**, *27*, 1410–1424. (In Chinese)

14. Huang, W.T.; Li, J.; Liang, H.Y.; Wang, C.L.; Lin, S.P.; Wang, X.Z. Zircon LA-ICP-MS U-Pb ages and highly oxidized features of magma associated with Luoboling porphyry Cu-Mo deposit in Zijinshan ore field, Fujian Province. *Acta Pet. Sin.* **2013**, *29*, 592–593. (In Chinese)
15. Xue, K. The Mineralization and Alteration Zonation of the Wuziqilong Copper Deposit in the Zijinshan Ore Field, Fujian Province. *Geotecton. Metallog.* **2013**, *37*, 463–470. (In Chinese)
16. Chen, J.; Chen, Y.J.; Zhong, J.; Sun, Y.; Qi, J.P.; Li, J. Geological and ore-fluid characteristics of Longjiangting Cu deposit in Zijinshan Orefield, Fujian Province, and their genetic implications. *Miner. Depos.* **2015**, *34*, 98–118. (In Chinese)
17. Pan, J.Y.; Ni, P.; Chi, Z.; Wang, W.B.; Zeng, W.C.; Xue, K. Alunite $^{40}Ar/^{39}Ar$ and Zircon U-Pb Constraints on the Magmatic-Hydrothermal History of the Zijinshan High-Sulfidation Epithermal Cu-Au Deposit and the Adjacent Luoboling Porphyry Cu-Mo Deposit, South China: Implications for Their Genetic Association. *Econ. Geol.* **2019**, *114*, 667–695. [CrossRef]
18. Jiang, S.H.; Bagas, L.; Liang, Q.L. New insights into the petrogenesis of volcanic rocks in the Shanghang Basin in the Fujian Province, China. *J. Asian Earth Sci.* **2015**, *105*, 48–67. [CrossRef]
19. Jiang, S.H.; Liang, Q.L.; Bagas, L.; Wang, S.H.; Nie, F.J.; Liu, Y.F. Geodynamic setting of the Zijinshan porphyry–epithermal Cu–Au–Mo–Ag ore system, SW Fujian Province, China: Constrains from the geochronology and geochemistry of the igneous rocks. *Ore Geol. Rev.* **2013**, *53*, 287–305. [CrossRef]
20. Zhao, J.H.; Hu, R.Z.; Zhou, M.F.; Liu, S. Elemental and Sr–Nd–Pb isotopic geochemistry of Mesozoic mafic intrusions in southern Fujian Province, SE China: Implications for lithospheric mantle evolution. *Geol. Mag.* **2007**, *144*, 937–952. [CrossRef]
21. Xiao, A.F.; Li, D.P.; Liu, X.M. LA-ICP-MS Zircon U-Pb Dating for the Volcanic Rocks of the Lower Formation of the Shimaoshan Group and Evolution of the Cretaceous Magmatism in the Zijinshan Cu-Au Orefield, Fujian Province. *Geotecton. Metallog.* **2012**, *36*, 613–623. (In Chinese)
22. Zhao, G.C.; Cawood, P.A. Precambrian geology of China. *Precambrian Res.* **2012**, *222–223*, 13–54. [CrossRef]
23. Zhang, S.B.; Zheng, Y.F. Formation and evolution of Precambrian continental lithosphere in South China. *Gondwana Res.* **2013**, *23*, 1241–1260. [CrossRef]
24. Chen, J.F.; Jahn, B.M. Crustal evolution of southeastern China: Nd and Sr isotopic evidence. *Tectonophysics* **1998**, *284*, 101–133. [CrossRef]
25. Xu, X.S.; O'Reilly, S.Y.; Griffin, W.L.; Wang, X.; Pearson, N.J.; He, Z.Y. The crust of Cathaysia: Age, assembly and reworking of two terranes. *Precambrian Res.* **2007**, *158*, 51–78. [CrossRef]
26. Zhou, J.C.; Jiang, S.Y.; Wang, X.L.; Yang, J.H.; Zhang, M.Q. Study on lithogeochemistry of Middle Jurassic basalts from southern China represented by the Fankeng basalts from Yongding of Fujian Province. *Sci. China Ser. D Earth Sci.* **2006**, *49*, 1020–1031. [CrossRef]
27. Liu, L.; Qiu, J.S.; Zhao, J.L.; Yang, Z.L. Geochronological, geochemical, and Sr–Nd–Hf isotopic characteristics of Cretaceous monzonitic plutons in western Zhejiang Province, Southeast China: New insights into the petrogenesis of intermediate rocks. *Lithos* **2014**, *196–197*, 242–260. [CrossRef]
28. Zhou, X.M.; Li, W.X. Origin of Late Mesozoic igneous rocks in Southeastern China: Implications for lithosphere subduction and underplating of mafic magmas. *Tectonophysics* **2000**, *326*, 269–287. [CrossRef]
29. Chen, C.H.; Lee, C.Y.; Lu, H.Y.; Hsieh, P.S. Generation of Late Cretaceous silicic rocks in SE China: Age, major element and numerical simulation constraints. *J. Asian Earth Sci.* **2008**, *31*, 479–498. [CrossRef]
30. Zhao, Z.F.; Gao, P.; Zheng, Y.F. The source of Mesozoic granitoids in South China: Integrated geochemical constraints from the Taoshan batholith in the Nanling Range. *Chem. Geol.* **2015**, *395*, 11–26. [CrossRef]
31. Li, L.M.; Sun, M.; Xing, G.F.; Zhao, G.C.; Zhou, M.F.; Wong, J.; Chen, R. Two late Mesozoic volcanic events in Fujian Province: Constraints on the tectonic evolution of southeastern China. *Int. Geol. Rev.* **2009**, *51*, 216–251. [CrossRef]
32. Li, B.; Jiang, S.Y. A subduction-related metasomatically enriched mantle origin for the Luoboling and Zhongliao Cretaceous granitoids from South China: Implications for magma evolution and Cu–Mo mineralization. *Int. Geol. Rev.* **2015**, *57*, 1239–1266. [CrossRef]
33. Zhao, J.H.; Hu, R.Z.; Liu, S. Geochemistry, Petrogenesis, and Tectonic Significance of Mesozoic Mafic Dikes, Fujian Province, Southeastern China. *Int. Geol. Rev.* **2010**, *46*, 542–557. [CrossRef]
34. Liu, Q.; Yu, J.H.; Wang, Q.; Su, B.; Zhou, M.F.; Xu, H.; Cui, X. Ages and geochemistry of granites in the Pingtan–Dongshan Metamorphic Belt, Coastal South China: New constraints on Late Mesozoic magmatic evolution. *Lithos* **2012**, *150*, 268–286. [CrossRef]

35. Huang, W.T. Study on Magmatism and Deposit Formation in the Zijinshan-Luoboling Mine Area, Fujian Province. Ph.D. Thesis, University of Chinese Academy of Sciences, Beijing, China, 2014.
36. Guo, F.; Fan, W.M.; Li, C.W.; Zhao, L.; Li, H.X.; Yang, J.H. Multi-stage crust–mantle interaction in SE China: Temporal, thermal and compositional constraints from the Mesozoic felsic volcanic rocks in eastern Guangdong–Fujian provinces. *Lithos* **2012**, *150*, 62–84. [CrossRef]
37. Zheng, K.L. New reseaching development of late Mesozoic volcano formation in Fujian Province. *Geol. Fujian* **2012**, *31*, 335. (In Chinese)
38. Zhang, D.Q.; She, H.Q.; Yan, S.H.; Xu, W.Y. Geochemistry of Mesozoic magmatities in the Zijinshan Region and implication on regional tectonic inversion. *Geol. Rev.* **2001**, *47*, 608–615. (In Chinese)
39. Liang, Q.L.; Jiang, S.H.; Wang, S.H.; Chen, C.L.; Liu, Y.F.; Bai, D.M. Petrogenesis of the Mesozoic magmatic rocks in Zijinshan area: Constraints from zircon Hf isotope evidence. *Acta Petrol. Mineral.* **2013**, *32*, 318–328. (In Chinese)
40. Geological and Environmental Reference Materials. Available online: http://georem.mpch-mainz.gwdg.de/ (accessed on 20 November 2019).
41. Liu, Y.S.; Hu, Z.C.; Zong, K.Q.; Gao, C.G.; Gao, S.; Xu, J.; Chen, H.H. Reappraisement and refinement of zircon U-Pb isotope and trace element analyses by LA-ICP-MS. *Chin. Sci. Bull.* **2010**, *55*, 1535–1546. [CrossRef]
42. Ludwig, K.R. *Isoplot 3.0: A Geochronological Toolkit for Microsoft Excel*; Berkeley Geochronology Center: Berkeley, CA, USA, 2003; p. 70.
43. Qi, L.; Hu, J.; Gregoire, D.C. Determination of trace elements in granites by inductively coupled plasma mass spectrometry. *Talanta* **2000**, *51*, 507–513.
44. Richard, P.; Shimizu, N.; Allegre, C. $^{143}Nd/^{146}Nd$, a natural tracer: An application to oceanic basalts. *Earth Planet. Sci. Lett.* **1976**, *31*, 269–278. [CrossRef]
45. Pu, W.; Zhao, K.D.; Ling, H.F.; Jiang, S.Y. High precision Nd isotope measurement by Triton TI Mass Spectrometry. *Acta Geosci. Sin.* **2004**, *25*, 271–274. (In Chinese)
46. Li, X.H.; Li, W.X.; Li, Q.L.; Wang, X.C.; Liu, Y.; Yang, Y.H. Petrogenesis and tectonic significance of the ~850 Ma Gangbian alkaline complex in South China: Evidence from in situ zircon U–Pb dating, Hf–O isotopes and whole-rock geochemistry. *Lithos* **2010**, *114*, 1–15. [CrossRef]
47. Wiedenbeck, M.; Hanchar, J.M.; Peck, W.H.; Sylvester, P.; Valley, J.; Whitehouse, M.; Kronz, A.; Morishita, Y.; Nasdala, L.; Fiebig, J.; et al. Further Characterisation of the 91500 Zircon Crystal. *Geostand. Geoanal. Res.* **2004**, *28*, 9–39. [CrossRef]
48. Patchett, P.J.; Tatsumoto, M. A Routine High-Precision Method for Lu-Hf Isotope Geochemistry and Chronology. *Contrib. Miner. Pet.* **1980**, *75*, 263–267. [CrossRef]
49. Machado, N.; Simonetti, A. U-Pb dating and Hf isotopic composition of zircon by Laser Ablation-MC-ICP-MS. *Laser-Ablation-Icpms Earth Sci. Princ. Appl. Can.* **2001**, *29*, 121–146.
50. Vervoort, J.D.; Patchett, P.J.; Söderlund, U.; Baker, M. Isotopic composition of Yb and the determination of Lu concentrations and Lu/Hf ratios by isotope dilution using MC-ICPMS. *Geochem. Geophys. Geosyst.* **2004**, *5*, 1–15. [CrossRef]
51. Chi, Z.; Ni, P.; Liao, J.F.; Fan, M.S.; Liu, Z.; Zhang, X. The comparative study of the geochemistry of Wenwu porphyry and Luoboling porphyry in Zijinshan ore-field, Fujian province. *J. Nanjing Univ.* **2018**, *54*, 398–412. (In Chinese)
52. Jacques, G.; Hoernle, K.; Gill, J.; Hauff, F.; Wehrmann, H.; Garbe-Schönberg, D.; van den Bogaard, P.; Bindeman, I.; Lara, L.E. Across-arc geochemical variations in the Southern Volcanic Zone, Chile (34.5–38.0° S): Constraints on mantle wedge and slab input compositions. *Geochim. Cosmochim. Acta* **2013**, *123*, 218–243. [CrossRef]
53. Rapp, R.P.; Shimizu, N.; Norman, M.D.; Applegate, G.S. Reaction between slab-derived melts and peridotite inthe mantle wedge: Experimental constraints at 3.8 GPa. *Chem. Geol.* **1999**, *160*, 335–356. [CrossRef]
54. Sun, S.S.; McDonough, W.F. Chemical and isotopic systematics of oceanic basalts: Implications for mantle composition and processes. *Geol. Soc. Lond. Spec. Publ.* **1989**, *42*, 313–345. [CrossRef]
55. Chen, J.Y.; Yang, J.H.; Zhang, J.H.; Sun, J.F.; Wilde, S.A. Petrogenesis of the Cretaceous Zhangzhou batholith in southeastern China: Zircon U–Pb age and Sr–Nd–Hf–O isotopic evidence. *Lithos* **2013**, *162–163*, 140–156. [CrossRef]
56. Zindler, A.; Hart, S.R. Chemical geodynamics. *Rev. Earth Planet. Sci.* **1986**, *14*, 493–571. [CrossRef]

57. Shen, W.Z.; Wang, D.Z.; Liu, C.S. Isotope geochemical characteristics and material sources of tin-bearing porphyries in South China. *Acta Geol. Sin.* **1996**, *9*, 181–192.
58. He, Z.Y.; Xu, X.S. Petrogenesis of the Late Yanshanian mantle-derived intrusions in southeastern China: Response to the geodynamics of paleo-Pacific plate subduction. *Chem. Geol.* **2012**, *328*, 208–221. [CrossRef]
59. Yu, J.S.; Gui, X.T.; Yuan, C. The characteristics of isotopes geochemistry of darongshan granitoid suite, Guangxi. *Geology* **1999**, *12*, 1–6. (In Chinese)
60. Qi, C.S.; Deng, X.G.; Li, W.X.; Li, X.H.; Yang, Y.H.; Xie, L.W. Origin of the Darongshan-Shiwandashan S-type granitoid belt from southeastern Guangxi: Geochemical and Sr-Nd-Hf isotopic constraints. *Acta Pet. Sin.* **2007**, *23*, 403–412.
61. Ayers, J. Trace element modeling of aqueous fluid-peridotite interaction in the mantle wedge of subduction zones. *Contrib. Min. Pet.* **1998**, *132*, 390–404. [CrossRef]
62. Plank, T.; Langmuir, C.H. The chemical composition of subducting sediment and its consequences for the crust and mantle. *Chem. Geol.* **1998**, *145*, 325–394. [CrossRef]
63. Jahn, B.M.; Wu, F.Y.; Lo, C.H.; Tsai, C.H. Crust–mantle interaction induced by deep subduction of the continental crust: Geochemical and Sr–Nd isotopic evidence from post-collisional mafic–ultramafic intrusions of the northern Dabie complex, central China. *Chem. Geol.* **1999**, *157*, 119–146. [CrossRef]
64. Hofmann, A.W.; Jochum, K.P.; Seufert, M.; White, W.M. Nb and Pb in oceanic basalts: New constraints on mantle evolution. *Earth Planet. Sci. Lett.* **1986**, *79*, 33–45. [CrossRef]
65. Keppler, H. Constraints from partitioning experiments on the composition of subduction-zone fluids. *Nature* **1996**, *380*, 237–240. [CrossRef]
66. Rudnick, R.L.; Gao, S. Composition of the Continental Crust. In *Treatise on Geochemistry*, 2nd ed.; Elsevier: Amsterdam, The Netherlands, 2014; pp. 1–51.
67. Jiang, S.H.; Bagas, L.; Liang, Q.L. Pyrite Re-Os isotope systematics at the Zijinshan deposit of SW Fujian, China: Constraints on the timing and source of Cu-Au mineralization. *Ore Geol. Rev.* **2017**, *80*, 612–622. [CrossRef]
68. Hu, G.R.; Zhang, B.D. Neodymium isotope compositions and source materials of the meta-basement in Central Jiangxi Province. *Acta Petrol. Mineral.* **1998**, *17*, 35–40. (In Chinese)
69. Rapp, R.P.; Watson, E.B. Dehydration Melting of Metabasalt at 8–32 kbar: Implications for Continental Growth and Crust-Mantle Recycling. *J. Pet.* **1995**, *36*, 891–931. [CrossRef]
70. Rutter, M.J.; Wyllie, P.J. Melting of vapour-absent tonalite at 10 kbar to simulate dehydration-melting in the deep crust. *Nature* **1988**, *331*, 159–160. [CrossRef]
71. Green, T.H. Significance of Nb/Ta as an indicator of geochemical processes in the crust-mantle system. *Chem. Geol.* **1995**, *120*, 347–359. [CrossRef]
72. Mcdonough, W.F.; Sun, S.S. The composition of the earth. *Chem. Geol.* **1995**, *120*, 223–253. [CrossRef]
73. Li, Z.; Qiu, J.S.; Yang, X.M. A review of the geochronology and geochemistry of Late Yanshanian (Cretaceous) plutons along the Fujian coastal area of southeastern China: Implications for magma evolution related to slab break-off and rollback in the Cretaceous. *Earth-Sci. Rev.* **2014**, *128*, 232–248. [CrossRef]
74. Kemp, A.I.S.; Hawkesworth, C.J.; Foster, G.L.; Paterson, B.A.; Woodhead, J.D.; Hergt, J.M.; Gray, C.M.; Whitehouse, M.J. Magmatic and crustal differentiation history of granitic rocks from hafnium and oxygen isotopes in zircon. *Science* **2007**, *315*, 980–983. [CrossRef]
75. Valley, J.W.; Lackey, J.S.; Cavosie, A.J.; Clechenko, C.C.; Spicuzza, M.J.; Basei, M.A.S.; Bindeman, I.N.; Ferreira, V.P.; Sial, A.N.; King, E.M.; et al. 4.4 billion years of crustal maturation: Oxygen isotope ratios of magmatic zircon. *Contrib. Miner. Pet.* **2005**, *150*, 561–580. [CrossRef]
76. Meng, L.; Li, Z.X.; Chen, H.L.; Li, X.H.; Wang, X.C. Geochronological and geochemical results from Mesozoic basalts in southern South China Block support the flat-slab subduction model. *Lithos* **2012**, *132–133*, 127–140. [CrossRef]
77. Pearce, J.A.; Peate, D.W. Tectonic implications of the compositions of volcanic arc magmas. *Annu. Rev. Earth Planet. Sci.* **1995**, *23*, 251–285. [CrossRef]
78. Li, P.J.; Yu, X.Q.; Li, H.Y.; Qiu, J.T.; Zhou, X. Jurassic–Cretaceous tectonic evolution of Southeast China: Geochronological and geochemical constraints of Yanshanian granitoids. *Int. Geol. Rev.* **2013**, *55*, 1202–1219. [CrossRef]
79. Hofmann, A.W. Mantle geochemistry: The message from oceanic volcanism. *Nature* **1997**, *385*, 219–229. [CrossRef]

80. Sun, W.D.; Hu, Y.H.; Kamenetsky, V.S.; Eggins, S.M.; Chen, M.; Arculus, R.J. Constancy of Nb/U in the mantle revisited. *Geochim. Cosmochim. Acta* **2008**, *72*, 3542–3549. [CrossRef]
81. Li, Z.X.; Li, X.H. Formation of the 1300-km-wide intracontinental orogen and postorogenic magmatic province in Mesozoic South China: A flat-slab subduction model. *Geology* **2007**, *35*, 179–182. [CrossRef]
82. Kelemen, P.B.; Hanghoj, K.; Greene, A.R. One View of the Geochemistry of Subduction-Related Magmatic Arcs, with an Emphasis on Primitive Andesite and Lower Crust. *Treatise Geochem.* **2007**, *138*, 1–70.
83. Conticelli, S.; Guarnieri, L.; Farinelli, A.; Mattei, M.; Avanzinelli, R.; Bianchini, G.; Boari, E.; Tommasini, S.; Tiepolo, M.; Prelevic, D. Trace elements and Sr-Nd-Pb isotopes of K-rich, shoshonitic, and calc-alkaline magmatism of the Western Mediterranean region: Genesis of ultrapotassic to calc-alkaline magmatic associations in a post-collisional geodynamic setting. *Lithos* **1999**, *107*, 68–92. [CrossRef]
84. Lloyd, F.E.; Arima, M.; Edgar, A.D. Partial melting of a phlogopite-clinopyroxenite nodule from south-west Uganda: An experimental study bearing on the origin of highly potassic continental rift volcanics. *Contrib. Miner. Pet.* **1985**, *91*, 321–329. [CrossRef]
85. Baker, M.B.; Hirschmann, M.M.; Ghiorsot, M.S.; Stolper, E.M. Compositions of near-solidus peridotite melts from experiments and thermodynamic calculations. *Nature* **1995**, *375*, 308–311. [CrossRef]
86. Schmidt, M.W.; Jagoutz, O. The global systematics of primitive arc melts. *Geochem. Geophys. Geosyst.* **2017**, *18*, 2817–2854. [CrossRef]
87. Xu, Y.; Xu, L.L.; Bi, X.W.; Hu, R.Z.; Chen, X.L.; Ma, R.; Zhu, J.J.; Yu, H.J.; Liu, B.H.; Li, J. Petrogenesis and metallogenic implications of volcanic rocks from the Lawu basin, eastern Tibet: Insights into the intracontinental Eocene-Oligocene porphyry copper systems. *Ore Geol. Rev.* **2019**, *111*, 1–27. [CrossRef]
88. Gudnason, J.; Holm, P.M.; Søager, N.; Llambías, E.J. Geochronology of the late Pliocene to recent volcanic activity in the Payenia back-arc volcanic province, Mendoza Argentina. *J. S. Am. Earth Sci.* **2012**, *37*, 191–201. [CrossRef]
89. Ballard, J.R.; Palin, M.J.; Campbell, I.H. Relative oxidation states of magmas inferred from Ce(IV)/Ce(III) in zircon: Application to porphyry copper deposits of northern Chile. *Contrib. Miner. Pet.* **2002**, *144*, 347–364. [CrossRef]
90. Richards, J.P. Tectono-Magmatic Precursors for Porphyry Cu-(Mo-Au) Deposit Formation. *Econ. Geol.* **2003**, *98*, 1515–1533. [CrossRef]
91. Loucks, R.R. Distinctive composition of copper-ore-forming arc magmas. *Aust. J. Earth Sci.* **2014**, *61*, 5–16. [CrossRef]
92. De Hoog, J.C.M.; Hattori, K.H.; Hoblitt, R.P. Oxidized sulfur-rich mafic magma at Mount Pinatubo, Philippines. *Contrib. Miner. Pet.* **2003**, *146*, 750–761. [CrossRef]
93. John, H.D.; Adam, J.R.K.; Joseph, L.W.; Richard, M.T.; Alison, K.; Robert, G.L.; Lucian, P.F. Zircon compositional evidence for sulfur-degassing from ore-forming arc magmas. *Econ. Geol.* **2015**, *110*, 241–251.
94. Lu, Y.J.; Loucks, R.R.; Fiorentini, M.L.; Mccuaig, T.C.; Evans, N.J.; Yang, Z.M.; Hou, Z.Q. Zircon Compositions as a pathfinder for Porphyry Cu± Mo± Au Deposits. *Soc. Econ. Geol. Spec. Publ. Ser.* **2016**, *19*, 329–347.
95. Li, X.Y.; Gao, Q.Z.; Song, H.; Zhang, J.R.; Lai, C.K. Discriminating ore fertile and barren granites using zircon Ce and Eu anomalies—Perspective from late Mesozoic (Yanshanian) granites in South China. *Ore Geol. Rev.* **2019**, *113*, 1644. [CrossRef]
96. Zhu, J.J.; Richards, J.P.; Rees, C.; Creaser, R.; DuFrane, S.A.; Locock, A.; Petrus, J.A.; Lang, J. Elevated Magmatic Sulfur and Chlorine Contents in Ore-Forming Magmas at the Red Chris Porphyry Cu-Au Deposit, Northern British Columbia, Canada. *Econ. Geol.* **2018**, *113*, 1047–1075. [CrossRef]
97. Wang, R.; Richards, J.P.; Hou, Z.Q.; Yang, Z.M.; Gou, Z.B.; Dufrane, S.A. Increasing magmatic oxidation state from Paleocene to Miocene in the eastern Gangdese belt, Tibet: Implication for collision-related porphyry Cu-Mo±Au mineralization. *Econ. Geol.* **2014**, *109*, 1943–1965. [CrossRef]
98. Toplis, M.J.; Carroll, M.R. An Experimental Study of the Influence of Oxygen Fugacity on Fe-Ti Oxide Stability, Phase Relations, and Mineral–Melt Equilibria in Ferro-Basaltic Systems. *J. Pet.* **1995**, *36*, 1137–1170. [CrossRef]
99. Park, J.W.; Campbell, I.H.; Arculus, R.J. Platinum-alloy and sulfur saturation in an arc-related basalt to rhyolite suite: Evidence from the Pual Ridge lavas, the Eastern Manus Basin. *Geochim. Cosmochim. Acta* **2013**, *101*, 76–95. [CrossRef]

100. Park, J.W.; Campbell, I.H.; Kim, J.; Moon, J.W. The Role of Late Sulfide Saturation in the Formation of a Cu- and Au-rich Magma: Insights from the Platinum Group Element Geochemistry of Niuatahi–Motutahi Lavas, Tonga Rear Arc. *J. Pet.* **2015**, *56*, 59–81. [CrossRef]
101. Jenner, F.E.; Hauri, E.H.; Bullock, E.S.; König, S.; Arculus, R.J.; Mavrogenes, J.A.; Mikkelson, N.; Goddard, C. The competing effects of sulfide saturation versus degassing on the behavior of the chalcophile elements during the differentiation of hydrous melts. *Geochem. Geophys. Geosyst.* **2015**, *16*, 1490–1507. [CrossRef]
102. Hao, H.D.; Campbell, I.H.; Park, J.W.; Cooke, D.R. Platinum-group element geochemistry used to determine Cu and Au fertility in the Northparkes igneous suites, New South Wales, Australia. *Geochim. Cosmochim. Acta* **2017**, *216*, 372–392. [CrossRef]
103. Richards, J.P. Magmatic to hydrothermal metal fluxes in convergent and collided margins. *Ore Geol. Rev.* **2011**, *40*, 1–26. [CrossRef]
104. Richards, J.P.; Kerrich, R. Adakite-like rocks; their diverse origins and questionable role in metallogenesis. *Econ. Geol.* **2007**, *102*, 537–576. [CrossRef]
105. Richards, J.P. High Sr/Y arc magmas and porphyry Cu ± Mo ± Au deposits: Just add water. *Econ. Geol.* **2011**, *106*, 1075–1081. [CrossRef]
106. Sun, W.D.; Huang, R.F.; Li, H.; Hu, Y.B.; Zhang, C.C.; Sun, S.J.; Zhang, L.P.; Ding, X.; Li, C.Y.; Zartman, R.E.; et al. Porphyry deposits and oxidized magmas. *Ore Geol. Rev.* **2015**, *65*, 97–131. [CrossRef]
107. Hou, Z.Q.; Yang, Z.M.; Lu, Y.J.; Kemp, A.; Zheng, Y.C.; Li, Q.Y.; Tang, J.X.; Yang, Z.S.; Duan, L.F. A genetic linkage between subduction-and collision-related porphyry Cu deposits in continental collision zones. *Geology* **2015**, *43*, 247–250. [CrossRef]
108. Richards, J.P. The oxidation state, and sulfur and Cu contents of arc magmas: Implications for metallogeny. *Lithos* **2015**, *233*, 27–45. [CrossRef]
109. Sun, W.D.; Liang, H.Y.; Ling, M.X.; Zhan, M.Z.; Ding, X.; Zhang, H.; Yang, X.Y.; Li, Y.L.; Ireland, T.R.; Wei, Q.R.; et al. The link between reduced porphyry copper deposits and oxidized magmas. *Geochim. Cosmochim. Acta* **2013**, *103*, 263–275. [CrossRef]
110. Jugo, P.J. Sulfur content at sulfide saturation in oxidized magmas. *Geology* **2009**, *37*, 415–418. [CrossRef]
111. Sun, W.D.; Bennett, V.C.; Kamenetsky, V.S. The mechanism of Re enrichment in arc magmas: Evidence from Lau Basin basaltic glasses and primitive melt inclusions. *Earth Planet. Sci. Lett.* **2004**, *222*, 101–114. [CrossRef]
112. Richard, J.P. Postsubduction porphyry Cu-Au and epithermal Au deposits: Products of remelting of subduction-modified lithosphere. *Geology* **2009**, *37*, 247–250. [CrossRef]
113. Mengason, M.J.; Candela, P.A.; Piccolip, M. Molybdenum, tungsten and magganese partitioning in the system pyrrhotite-Fe-S-O melt-rhyolite melt: Impact of sulfide segregation on arc magma evolution. *Geochim. Cosmochim. Acta* **2011**, *75*, 7018–7030. [CrossRef]